

## Article

# Corrosion Behaviour of Cemented Carbides with Co- and Ni-Alloy Binders in the Presence of Abrasion

Gian Pietro De Gaudenzi <sup>1</sup>, Francesco Tavola <sup>2</sup>, Sandra Tedeschi <sup>1</sup> and Benedetto Bozzini <sup>2,\*</sup> <sup>1</sup> F.I.L.M.S. S.p.A.—OMCD Group, 28877 Anzola d'Ossola, Italy<sup>2</sup> Dipartimento di Energia, Politecnico di Milano, Via Lambruschini 4, 20156 Milano, Italy

\* Correspondence: benedetto.bozzini@polimi.it

**Abstract:** More and more often, cemented carbides are employed for the production of wear resistant components and have to face highly demanding service conditions that combine different damage mechanisms. A key example is the range of tetraphasic (sea water, sand, liquid and gaseous hydrocarbons) flows encountered in the Oil and Gas extraction industry. Notwithstanding the importance of operating regimes of this type, the availability of fundamental and quantitative information on the corrosion performance of cemented carbides in the presence of abrasion is still limited. In this paper, we report a systematic study of the corrosion behaviour of cemented tungsten carbide grades with binders containing different amounts of cobalt (Co), nickel (Ni), chromium (Cr) and noble metal additions, subjected to controlled mechanical abrasion, impacting the stability and nature of pseudopassivation films. In this work, special attention is devoted to Cr, a classical additive that inhibits the Ostwald ripening of tungsten carbide (WC) particles and notably improves the corrosion resistance of grades with ultrafine-to-fine WC grain size and low-to-medium binder content. We assessed the impact of binder composition on the anodic behaviour by means of linear-sweep voltammetry and chronopotentiometry as well as on the mechanical properties. The application of controlled abrasion conditions under electrochemical control is carried out with an in-house modified ASTM B611 apparatus, equipped with a three-electrode system, enabling the systematic investigation of the synergy of electrochemical and mechanical damaging conditions. Increased corrosion resistance in environments without and with added chloride—both in the absence and in the presence of abrasion—was observed in all the Co- and Ni-based grades to which growing quantities of Cr were added. Moreover, doping with ruthenium (Ru) further enhances corrosion resistance. Regarding corrosion in the presence of abrasion, the addition of Cr and Ru increases the ability of regenerating the pseudopassivation film. The optimized compositions of the binder have been highlighted that open up attractive opportunities of improved service behaviour and deployment in new applications.

**Keywords:** cemented carbide; abrasion; corrosion; abrasion–corrosion; binder additives; binder alloys

**Citation:** De Gaudenzi, G.P.; Tavola, F.; Tedeschi, S.; Bozzini, B. Corrosion Behaviour of Cemented Carbides with Co- and Ni-Alloy Binders in the Presence of Abrasion. *Metals* **2022**, *12*, 1914. <https://doi.org/10.3390/met12111914>

Academic Editors: Haiming Ding, Peng Wang and Xiangguang Kong

Received: 28 September 2022

Accepted: 2 November 2022

Published: 8 November 2022

**Publisher's Note:** MDPI stays neutral with regard to jurisdictional claims in published maps and institutional affiliations.



**Copyright:** © 2022 by the authors. Licensee MDPI, Basel, Switzerland. This article is an open access article distributed under the terms and conditions of the Creative Commons Attribution (CC BY) license (<https://creativecommons.org/licenses/by/4.0/>).

## 1. Introduction

Cemented carbides (CCs) feature outstanding properties that make them a strategic class of materials for industrial economy. CCs were originally developed mainly for the production of cutting and forming tools [1], but, during their centennial history, and in particular in the last decades, they have been involved in an increasingly wider range of applications as material for wear-resistant components. For this reason, the wear mechanisms of CCs were extensively studied and modelled [2]. As summarized by Gee et al. [3], the wear process occurs through sequential steps: the removal of the binder phase from the surface of the component; the plastic deformation and grooving of the remaining metal; the accumulation of plastic deformation in the WC grains, their fragmentation and eventually the re-embedding of fragments into the binder; and the cracking between WC grains and the breakaway of unsupported grains. Nonetheless, in many of its newer applications, CCs also experience serious chemical interactions with the environment. Over the last 25 years,

the understanding of the CC corrosion mechanisms has notably deepened in some niche studies, as reviewed in [4]. The electronic conductivity of WC causes the CC composite in contact with an electrolyte to behave as a multimetallic object, the corrosion process of which is dominated by galvanic coupling. This results in the establishment of two complementary reactions: the anodic oxidation of the binder and the cathodic reduction of aggressive species present in the environment, which occurs at the surface of the WC phase. These studies highlighted a so-called pseudopassivation (PP) behaviour that controls the corrosion performance of CC grades through the metallurgical details of the metallic binder [4]. More recently, advanced spectrometric and spectro-electrochemical methods have been adopted for the investigation of the CC/electrolyte interface [4,5]. This approach allowed the identification of the active sites on the material surface and the molecular details of the interaction of solution species with the CC surface. Notwithstanding notable progress in fundamental understanding, a comprehensive view of PP phenomena is still to be achieved: in particular, a missing piece of information is the impact of wear conditions on the stability, formation rate and nature of PP films (PPFs). More in general, from the point of view of CC as a system, even tribocorrosion is still in its infancy, notwithstanding solid recent methodological developments. Mischler et al. [6–8] have highlighted the synergistic impact of wear and corrosion on passivation behaviour. Landolt et al. [9] reviewed the requirements for the rigorous execution of these kinds of measurements. Wood et al. [10] introduced mechano-electrochemical plots to enable a better understanding of the mutual role of the two interacting mechanisms and to predict material performance: this work is one of the few examples (e.g., [11]) of tribocorrosion studies on CCs in the classical sense.

Among different kinds of mechanical action affecting corrosion performance, one of the technically most critical for CCs is abrasion in the Oil and Gas industry. In this field, the surface of performance- and safety-crucial CC components is exposed to highly aggressive multi-phase—typically tetraphasic (seawater, liquid hydrocarbon, gaseous hydrocarbon and sand)—flows. The synergistic effect of exposure to this particular ambient is the abrasion damaging of the PPFs, accompanied by the weakening of the WC skeleton on the freshly exposed surfaces, due to the selective corrosion of the metallic binder. In applications for wear and corrosion resistance, Cr has been playing a key role in the development of hard metals since the very beginning of their industrial applications, when research at Krupp showed that it enabled the production of harder CCs: the so-called class “H” grades [1,12]. Although at the end of the 1960s, Cr was still believed to have a detrimental effect on the transverse rupture strength [13], by the 1980s the knowledge of its beneficial effect on the corrosion behaviour in Ni-based hard metals was consolidated [14,15]. In the 1990s, with the advent of the sub-micron and ultrafine WC era, the role of chromium as a grain-growth inhibitor was definitively highlighted [12,16,17] and some interesting studies were undertaken to pinpoint the mechanism of WC grain-growth inhibition and the influence on WC crystal morphology [18,19]. Since the end of the 1990s, as a result, on the one hand, regarding the evolution of Electrical Discharge Machining (EDM) cutting procedures [20] and, on the other hand, regarding the extension of CC applications in different environments, some research groups have been deepening the corrosion mechanisms of hard metals and started addressing the synergy of electrochemical and mechanical factors [21,22]. Thus, in view of the improvement of corrosion resistance, the addition of Cr to both Co- and Ni-based grades is experiencing renewed interest [23]. The good solubility of Cr in the Co- or Ni-based matrix has been known since the early hard metal age [1]. The measurement of the solubility value of Cr has been the focus of dedicated research, aimed at understanding how to maximize the contribution of this addition element to the HM properties, avoiding at the same time the precipitation of carbides, such as  $M_7C_3$  and  $\eta$ -phase  $M_6C$  ( $M = Cr, Co, W$ ), which are detrimental to mechanical properties. Etmayer and coworkers at TU Wien reported the solubility values of Cr in Co of 5 wt% and 12 wt% at 1000 °C and 1250 °C, respectively, in the presence of high carbon potentials [24]. In these conditions, if the solubility limit is exceeded, the first carbide to precipitate is  $M_7C_3$ , while in decarburized conditions,  $M_6C$  carbides

form. Zackrisson et al. [25] essentially confirmed Etmayer's results regarding carbide precipitation in high carbon activity conditions. More recently, the development of software and databases for the evaluation of thermodynamic quantities in complex systems, such as the Calphad framework, together with the availability of high-precision Differential Thermal Analysis (DTA) and Thermo-Gravimetric Analysis (TGA) instrumentation for the measurement of thermal parameters, have fostered a surge of predictive studies of phase composition [26,27]. According to the calculations of K. Frisk and A. Markström, in particular, the Cr solubility values in high C content HM are 11.9 wt% and 6.9 wt% at 1191 and 1190 °C, respectively, i.e., with and without the presence of a liquid phase. R. de Oro Calderon reported 7 wt% solubility of Cr in a high carbon-content 20 wt% Co grade, with the formation of  $M_7C_3$  carbides [28]. In recent years, the role of Cr as an additive has been progressively extending to grades with progressively higher binder content. As far as the solubility of Cr in Ni-base grades is concerned, de Oro Calderon at TU Wien also reported a value of 11 wt% in low-carbon conditions [28] and 9 wt% with a high carbon-content, yielding graphite and  $Cr_3C_2$  [29].

In order to improve mechanical and corrosion performance of hard metal grades, further alloying elements have been considered in CC design. Ruthenium is a noble metal, forming a solid solution with the cobalt in the binder phase, promoting the allotropic transformation of cobalt from cubic to hexagonal [30]. As a consequence, Ru has been shown to decrease toughness [31], although it increases hardness and abrasion resistance. Furthermore, Ru solution in Co decreases the magnetic moment at saturation [32] (see Table 1). Hafnium carbide is a highly refractory compound ( $T_m = 3900$  °C), promoting high hardness and corrosion resistance, thanks to its contribution to a passivation mechanism, giving rise to highly stable passivation films (e.g., in superalloys) [33]. In CCs, Hf precipitates as a  $\gamma$ -phase, such as Ti, Ta, Nb and Zr carbides, and plays a role similar to that of these valve-metals [12,33].

**Table 1.** Composition and metallurgical characterization of Co- and Ni-based grades, with Cr, Hf and Ru additions. MB: metallic binder content; MMS: relative magnetic moment at saturation; TRS: transverse rupture strength, PT: Palmqvist toughness.

Material	Metallic Binder	Additive Carbide	[MB] (wt%)	WC Grain Size	Density ( $\times 10^3$ kg m <sup>-3</sup> )	Hardness (HV30)	MMS (%)	TRS (MPa)	PT (MN m <sup>-3/2</sup> )
A	Co	-	8	s	14.72 ± 0.02	1679 ± 9	89 ± 1	3410 ± 90	9.5 ± 0.4
A <sub>1</sub>	Co	-	6	m	14.91 ± 0.03	1442 ± 15	87 ± 1	3345 ± 76	11.8 ± 0.5
B <sub>1</sub>	Co	-	9	m	14.58 ± 0.02	1291 ± 12	88 ± 1	3379 ± 112	18.2 ± 0.4
B	Co	-	10	m	14.46 ± 0.02	1398 ± 15	87 ± 1	3213 ± 64	18.0 ± 0.3
C	Co	-	15	m	14.02 ± 0.01	1256 ± 19	90 ± 1	3248 ± 99	>20
D	CoNiCr	-	15	m	13.98 ± 0.02	1246 ± 7	86 ± 1	3137 ± 121	>20
E	NiCr	-	8	f	14.69 ± 0.02	1400 ± 18	-	3118 ± 107	11.8 ± 0.3
C <sub>1</sub>	Co15Ru	-	6	m	14.85 ± 0.02	1530 ± 13	77 ± 1	3276 ± 124	10.6 ± 0.4
D <sub>1</sub>	Co	0.5HfC	6	m	14.82 ± 0.02	1490 ± 14	90 ± 1	3176 ± 94	9.7 ± 0.5
E <sub>1</sub>	Alloyed Ni	-	9	m	14.45 ± 0.03	n.d.	-	n.d.	n.d.

The present study jointly addresses the following issues, relevant to a systematic investigation of the interaction of mechanical and corrosion properties: (i) the development of an apparatus for applying controlled abrasion conditions during the electrochemical corrosion testing of CCs, based on the ASTM B611 standard abrasion testing; (ii) the ranking of CC grades that are candidates for Oil and Gas applications, and gaining the understanding of the self-healing attitude of PPFs on CC under abrasion; (iii) assessing systematically the role of Cr in high-binder content grades with respect to mechanical properties and mechano-chemical damaging.

## 2. Experimental

### 2.1. Sample Preparation

Two groups of grades were considered in this study. The CCs belonging to the first group are employed or are candidates for use in the Oil and Gas industry: their main features are reported in Table 1. This first group of CCs is a range of Co- and Ni-based grades, with Cr, Hf and Ru additions, including a grade with the Ni-base superalloy IN738LC employed as the metallic binder ( $E_1$ ). Powder mixtures were prepared via a standard powder-metallurgy route. Ultrafine Co powders by Umicore (Olen, Belgium), NI255 Ni powders by Vale/INCO (Clydach, UK) and IN738LC powders by H.C. Starck (Goslar, Germany) were used as base metallic binders. Cr was added as  $Cr_3C_2$  (by Treibacher Industrie AG, Althofen, Austria), Hf as HfC (by American Elements, Salt Lake City, UT, USA) and Ru as metallic powder (by American Elements). Powder mixtures underwent 48 h ball milling in ethyl alcohol. Samples were produced by pressing, de-waxing and pre-sintering and forming to the final geometry and finally sintering in a sinter-HIP furnace at 1360 °C and 1400 °C, in a 50-bar Ar atmosphere.

Cylindrical samples ( $\varnothing 12$  mm  $\times$  5 mm) were produced for electroanalytic measurements and prismatic samples (40 mm  $\times$  18 mm  $\times$  4 or 8 mm) for tribocorrosion tests.

The mechanical property data reported in Table 1 confirm the increase in hardness and the decrease in toughness due to Ru and HfC additions. In Figure 1, a selection of representative microstructures is shown. As expected, Ru is soluble in the Co-base metallic binder, while HfC precipitates as  $\gamma$ -phase.

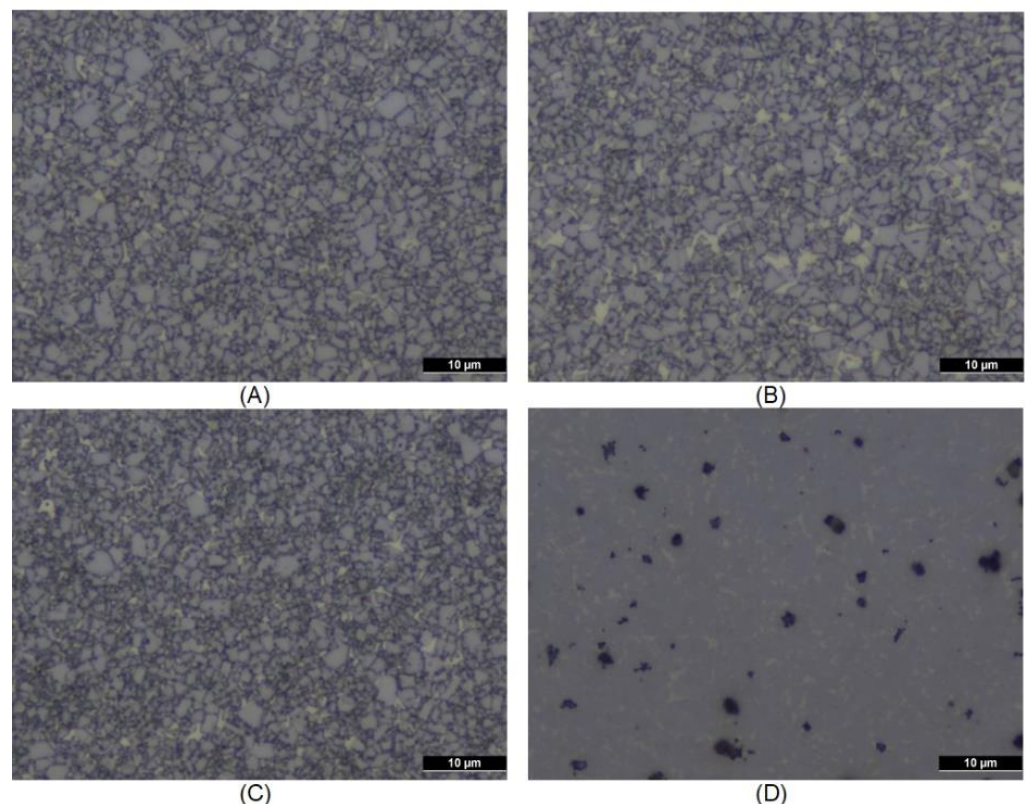


**Figure 1.** (A–C): the OM microstructures of grades of Table 1:  $A_1$  (WC-6Co),  $B_1$  (WC-9Co) and  $C_1$  (WC-6CoRu), respectively; (D): distribution of  $\gamma$ -phase (HfC) in grade  $D_1$  (WC-6CoHf).

The CCs belonging to the second group of grades, listed in Table 2, were prepared for a systematic investigation of Cr addition to Co- and Ni-based grades, employing the same Co, Ni and  $Cr_3C_2$  powders as raw materials, together with a 5- $\mu$ m WC (by Umicore SPF, Grenoble, France). The samples were fabricated with the same powder-metallurgy process described above. Furthermore, in order to systematically investigate the solubility

threshold, more compositions were considered, which will be discussed where relevant. All the Co- and Ni-base samples quoted in Table 2 were free from precipitated  $\eta$  carbides and graphite.

**Table 2.** Composition and metallurgical characterization of Co- and Ni-based grades, with a systematic variation of Cr content.

Batch	[Binder Base]	[Cr] <sub>binder</sub>	[Cr] <sub>HM</sub>	Density	Coercivity H <sub>c</sub>	Specific Magnetic Moment at Saturation $\sigma_s$	Abrasion Resistance (See Text) A
	m%	m%	m%	$\times 10^3 \text{ kg m}^{-3}$	kA m <sup>-1</sup>	$10^{-7} \text{ T m}^3 \text{ kg}^{-1}$	$10^{-11} \text{ m}^3 \text{ r}^{-1}$
584	Co 10	0	0	14.51 ± 0.02	8.28 ± 0.80	11.3 ± 0.2	22.7 ± 4.8
585	Co 10	3	0.3	14.46 ± 0.02	9.23 ± 0.72	10.4 ± 0.1	17.0 ± 4.3
586	Co 10	5	0.5	14.44 ± 0.02	10.03 ± 0.79	9.6 ± 0.1	14.1 ± 4.7
587	Co 15	0	0	14.02 ± 0.02	5.77 ± 0.59	11.5 ± 0.2	54.1 ± 5.6
588	Co 15	3	0.45	13.96 ± 0.01	6.84 ± 0.63	11.4 ± 0.2	43.6 ± 3.7
589	Co 15	5	0.75	13.91 ± 0.02	7.16 ± 0.65	10.4 ± 0.2	38.1 ± 4.6
590	Co 20	0	0	13.54 ± 0.01	4.91 ± 0.53	12 ± 0.2	91.0 ± 6.1
591	Co 20	3	0.6	13.48 ± 0.02	5.71 ± 0.55	10.8 ± 0.2	79.7 ± 1.8
592	Co 20	5	1.0	13.41 ± 0.02	5.78 ± 0.60	10.5 ± 0.2	69.0 ± 7.3
605	Co 20	8	1.6	13.32 ± 0.02	4.51 ± 0.51	10.3 ± 0.1	-
606	Co 20	10	2.0	13.29 ± 0.02	4.98 ± 0.40	10.1 ± 0.1	-
593	Co 25	0	0	13.10 ± 0.01	3.69 ± 0.37	12.4 ± 0.2	99.4 ± 2.9
594	Co 25	3	0.75	13.01 ± 0.02	4.40 ± 0.41	11.2 ± 0.2	92.7 ± 3.8
595	Co 25	5	1.25	12.95 ± 0.02	4.81 ± 0.48	11.4 ± 0.2	89.0 ± 4.1
596	Ni 15	0	0	14.05 ± 0.03	-	-	82.7 ± 2.5
597	Ni 15	3	0.45	13.95 ± 0.03	-	-	76.2 ± 2.9
598	Ni 15	5	0.75	13.89 ± 0.03	-	-	78.1 ± 2.6
599	Ni 15	8	1.2	13.79 ± 0.02	-	-	73.1 ± 2.7
600	Ni 15	10	1.5	13.75 ± 0.02	-	-	68.7 ± 1.0
607	Ni 15	12	1.8	13.87 ± 0.03	-	-	-
608	Ni 15	15	2.25	13.82 ± 0.03	-	-	-

## 2.2. Physical Characterization

Density and Vickers (30 kg) hardness were measured according to ISO 3369 and ISO 3878 standards, respectively. Coercivity H<sub>c</sub> and specific magnetic moment at saturation  $\sigma_s$  were assessed using a Foerster Koerzimat 1.096 magnetisation measuring system, according to ISO 3326 and ASTM B886 standards, respectively. The mean WC grain size of each grade was evaluated by the linear-intercept method, according to ISO 4499-2. The weight loss of some specimen and wear volume was evaluated according to ASTM B611.

The Palmqvist toughness was evaluated according to ISO 28079. The morphology and composition of pristine and tested surfaces were examined by optical and electronic microscopy, using a JSM-5500LV (Jeol, Tokyo, Japan) scanning electron microscope (SEM) equipped with Energy Dispersive X-ray Spectroscopy (EDS) (IXRF Systems, Austin, TX, USA).

The grain size distribution was evaluated employing the linear intercept method, according to ISO 4499-2 standard, using ImageJ (by NIH, Bethesda, MD, USA) as image processing software applied to BEI-SEM images. About 300 WC grains were considered for each sample.

## 2.3. The Abrasion–Corrosion Test System

A scheme of the apparatus for the abrasion–corrosion tests is shown in Figure 2. The mechanical design of this device is based on the ASTM B611 standard test instrument that

was equipped with a three-electrode system for electrochemical tests. Specifically, the working electrode (WE) consists in the specimen under study, isolated from the metallic frame that faces the steel wheel, which acts as the counter electrode (CE). It is worth emphasizing that, to the best of the Author's knowledge, this is the only tribocorrosion device exhibiting a current–density distribution design that enables electrochemical response principally from the mechanically attacked region, allowing high precision in the assessment of the mechano-electrochemical response. A corrosion resistant hard metal cylinder, exhibiting a high stability in time (drift less than 0.2 mV/h) of voltage against an Ag/AgCl RE in the solutions used, is employed as a quasi-reference electrode (RE). Specifically, during wheel rotation, the aluminium oxide grit slurry interposes between the specimen (WE) and the steel wheel (CE), dynamically establishing an electrochemical cell. During the tribocorrosion testing, the requirements of ASTM B611 standard (aluminium oxide grit, liquid/grit ratio, pressure of the specimen on the wheel and rotation speed) were fulfilled, apart from the electrolyte solution used and the time of each operating stage of the system, which are discussed in detail in Section 3.3 for each experiment. Abrasion–corrosion tests were carried out potentiostatically, but the system allows full flexibility, in principle enabling the use of all electroanalytic methods.

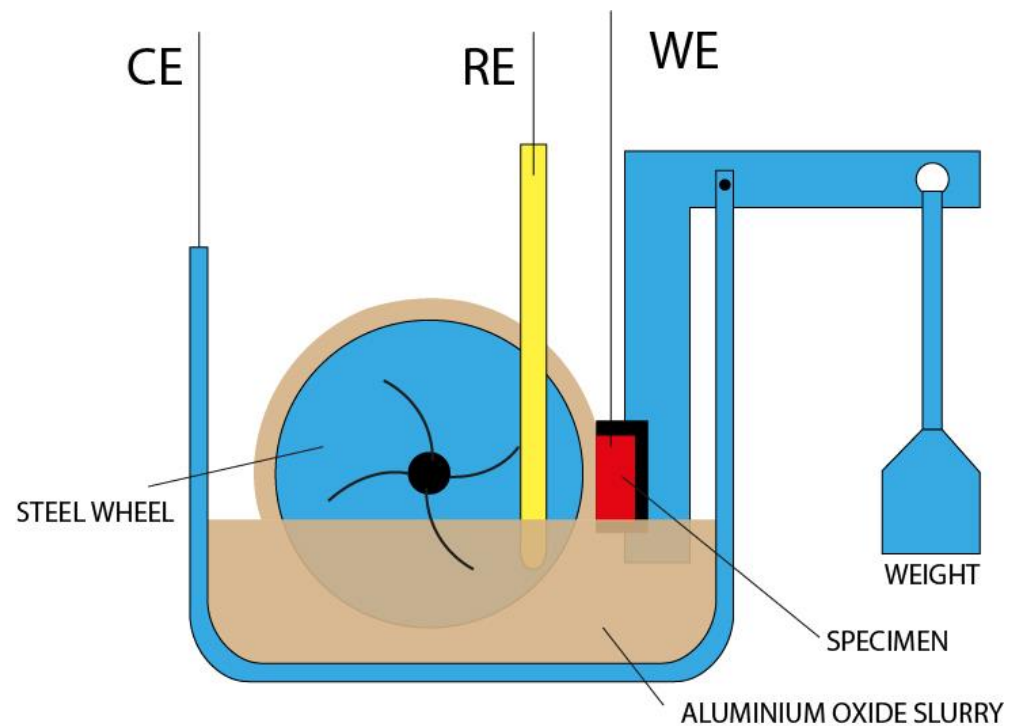


**Figure 2.** The modified ASTM B611 apparatus. The specimen is the working electrode (WE) and faces the steel wheel that acts as the counter electrode (CE); the slurry interposes between the sample and wheel, establishing the electrochemical cell. The dynamic layer of  $\text{Al}_2\text{O}_3$  grains, geometrically separating the WE and the CE, ensure electronic insulation, acting as a separator. The quasi-reference electrode (RE) is a corrosion-resistant hard metal rod.

Abrasion–corrosion tests were carried out in order to assess the synergistic effect of mechanical and chemical damaging processes, relevant to the Oil and Gas extraction industry. Potentiostatic or galvanostatic conditions were selected in order to emphasize the impact of a given level of oxidative power of the ambient or the energetics or the repassivation process, respectively. The slurry was formed by mixing the  $\text{Al}_2\text{O}_3$  particles required by the ASTM norm with electrolytes simulating some of the key characteristics of Oil and Gas extraction environments. Abrasion–corrosion tests consisted of a sequence of time intervals in which the abrading action is applied and ceased, alternatively.

A first set of measurements was carried out with samples A–E of Table 1 at appropriate potentials, detailed below. We adopted the following abrasion–corrosion sequence, involving three types of electrolyte for each CC grade. (i) *Interval without Cl<sup>−</sup> and without hydrocarbon*: here, 0.5 M Na<sub>2</sub>SO<sub>4</sub> aqueous solution was used for slurry formation; (i.a) 10 min rotation; (i.b) 13 min relaxation after stopping rotation; (i.c) rotation resumed for 7 min. (ii) *Interval with Cl<sup>−</sup> addition*: (ii.a) during rotation, the solution was rendered 0.6 M in NaCl by adding a concentrated NaCl that was quickly mixed with the tap-water based slurry, this method simulates the formation of the aqueous fraction of water in off-shore petrochemical extraction and rotation was continued for 10 more min; (ii.b) 13 min relaxation as above (point i.b); (ii.c) rotation resumed for 10 min. (iii) *Interval with hexane addition to the Cl<sup>−</sup>-containing slurry*: hexane was added to the slurry, again during rotation, in an amount that the organic phase corresponds to 20 vol% of the liquid fraction; this condition simulates the presence of a water-insoluble hydrocarbon phase in the oil extraction tetraphasic fluid. (iii.a) After organic addition, rotation was applied for 10 min, after which (iii.b) relaxation after stopping the rotation was measured. The total test duration was 83 min with a total 47 min under wheel rotation. As far as electrochemical control is concerned, potentiostatic conditions were applied till an anodic current density of 5 mA cm<sup>−2</sup> was attained—representative of fully developed active corrosion—after which the current was fixed to monitor the time evolution of the voltage required to keep active corrosion conditions.

#### 2.4. Linear Sweep Voltammetry Setups for Electrochemical Characterization

The electroanalytical characterization was performed by Linear Sweep Voltammetry (LSV) in a three-electrode cell with the CC WE in a hanging-meniscus configuration. The CEs were either a graphite rod or a platinized titanium mesh and the RE was an Ag/AgCl 3 M KCl electrode. Na<sub>2</sub>SO<sub>4</sub> 0.5 M and NaCl 0.6 M aqueous solution.

#### 2.5. Data Analysis

This section describes the simple but effective data-processing methods that were employed to extract quantitative information, where appropriate, from the corrosion and abrasion–corrosion measurements reported in this paper.

##### 2.5.1. Wear Volume

The wear volume  $V$  has been correlated with Vickers hardness  $H$  with the linear relationship proposed in Gant et al. [34]:

$$\log_{10} V = A - BH \quad (1)$$

where  $A$  and  $B$  are constants, characteristic of the investigated material and of the testing conditions.

##### 2.5.2. Steady-State Abrasion–Corrosion Performance

In order to quantitatively describe abrasion–corrosion experiment, we devised a simple model accounting for the impact of corrosion processes through Butler–Volmer electrokinetics and mechanical action via the removal of the PPF.

Neglecting the transpassive range, which is not relevant for most practical applications, in the Oil and Gas industry in particular, the LSV curves can be modelled using two approaches, detailed below.

A porosity model (in which the PPF is regarded as porous, yielding an effective surface coverage  $\theta_{max} < 1$ );

$$i(E) = i_0 \cdot \left\{ \exp\left[\frac{E-E_0}{B}\right] - \exp\left[-\frac{E-E_0}{B}\right] \right\} \cdot [1 - \theta(E)]$$

$$\theta(E) = \theta_{max} \cdot \left( 1 - \frac{1}{1 + \exp\left[\frac{E-E_1}{\Delta}\right]} \right) \quad (2)$$

where  $E$  is the applied potential,  $E_0$  the equilibrium potential,  $B$  the Tafel slope and  $1 - \theta$  the effective porosity of the PPF, modelled phenomenologically as a sigmoidal function of  $E$  with parameters  $E_1$  and  $\theta$ . The model, of course, accounts for the physically transparent limiting cases:

$$\begin{aligned} \lim_{E \rightarrow -\infty} \theta(E) &= 0 \\ \lim_{E \rightarrow \infty} \theta(E) &= \theta_{max} \end{aligned} \quad (3)$$

and

$$\begin{aligned} i(E_0) &= 0 \\ \lim_{v \rightarrow \infty} i(E) &\approx i_0 \cdot \exp\left[\frac{E-E_0}{B}\right] \cdot [1 - \theta_{max}] \end{aligned} \quad (4)$$

Representing, respectively, the high-cathodic (no PPF) and high-anodic (asymptotic PP) limits. Specifically, the analytical form of  $\theta(E)$  has the following meaning: the PPF exhibits a sigmoidal behaviour, characterized by a critical potential  $E_1$ , such that  $\theta(E_1) = \theta_{max}/2$  and a transition width  $\theta$ . Of course, this form of  $\theta(E)$  still results in an exponentially growing  $i(E)$ , but the absolute value is strongly lowered by the presence of the film.

A resistivity model, in which the pseudopassive film can attain full coverage ( $\theta = 1$ ), but it exhibits a finite resistance  $R$ .

$$\begin{aligned} i(E) &= i_0 \cdot \left\{ \exp\left[\frac{E-E_0}{B}\right] - \exp\left[\frac{E-E_0}{B}\right] \right\} \cdot [1 - \theta(E)] + \theta(E) \cdot \frac{E-E_0}{R} \\ \theta(E) &= 1 - \frac{1}{1 + \exp\left[\frac{E-E_1}{\Delta}\right]} \\ [1 - \theta(E)] &= \frac{1}{1 + \exp\left[\frac{E-E_1}{\Delta}\right]} \end{aligned} \quad (5)$$

where  $R$  is the effective resistance of the PPF. The resistance term is assumed to be activated as soon as the faradaic reaction starts; very close to  $E = E_0$  the linear correction, that sums to the linearized BV equation, boils down to a slight (in fact negligible, since typically  $E_1 > E_0$  and thus  $\theta(E \approx E_0) \approx 0$ ) underestimate the Tafel slope. Again, the physically evident limiting cases are incorporated into the model:

$$\begin{aligned} \lim_{v \rightarrow -\infty} \theta(E) &= 0 \\ \lim_{v \rightarrow \infty} \theta(E) &= 1 \end{aligned} \quad (6)$$

and

$$\begin{aligned} i(E_0) &= 0 \\ \lim_{v \rightarrow \infty} i(E) &\approx \frac{E-E_0}{R} \end{aligned} \quad (7)$$

### 2.5.3. Transient Abrasion–Corrosion Performance

Since the synergistic mechano-electrochemical processes controlling abrasion–corrosion ultimately depend on PPF removal and re-growth dynamics, transient-state measurements are required to convey a comprehensive view of the relevant damaging phenomena. In particular, materials can be transparently ranked by assigning to each of them an effectively removed PPF fraction  $R_{PP}$ , which is associated with the ability of each material to maintain its corrosion resistance during abrasion. This parameter is defined as:

$$R_{PP} = \frac{I_C}{I_B} \quad (8)$$

where  $I_B$  is the corrosion current of the bare metal (i.e., in the absence of PPF) extracted from the LSV data, while  $I_C$  is the corrosion current extracted from the potentiostatic current transient, which is independent to the variations of the geometrical area. In particular,  $I_C$  describes the corrosion rate of the material subjected to the relevant abrasion conditions.

In addition, characteristic relaxation times of the current, associated both with the current growth during abrasion and current decay when abrasion is stopped, can be obtained by fitting the current transients with a bi-exponential function, characterized by the time-constants reported in Table 3.

**Table 3.** The time constants of the bi-exponential function employed to fit current growth and decay during transients.

<b>Current growth</b>	$\tau_{\uparrow 1}$ Fast component associated with the mechanical removal of the PPF. $\tau_{\downarrow 1}$ Slow component associated with the mechanical damaging of the bare composite.
<b>Current decay</b>	$\tau_{\uparrow 2}$ Fast component associated with the build-up of the surface coverage with the PPF. $\tau_{\downarrow 2}$ Slow component associated with the growth of the resistive film.

### 3. Discussion and Results

#### 3.1. Abrasion Resistance

##### 3.1.1. Co-, CoNi- and CoNiCr-Based Grades

In order to assess the impact of Co binder content and Ni and Cr additions on abrasion resistance, the wear volume was evaluated from weight losses and density for grades A–E of Table 1. The results are reported in Table 4. Since these experiments were essentially meant as a confirmation of the expected trend and the quality of quantitation is not essential for the specific purpose of this study, at variance with all other data reported in this work, no replicated measurements were carried out. In spite of the fact that the test duration was five times that recommended in normal ASTM B611, the correlation between hardness and abrasion behaviour of Equation (1) has been found to hold (Figure 3). Figure 4 shows a typical example of a worn microstructure, characterized by the fracture of the large WC grains. Multiple cracks in individual grains are parallel and can be related more to the abrasion path than to the crystallographic axes of the crystal [34].

**Table 4.** Wear losses and wear volume for the indicated grades of Table 1.

Material	A	B	C	D	E
Weight loss	1.2678	4.1363	9.6851	5.9901	3.8484
Wear volume	0.0862	0.2853	0.6918	0.4279	0.2618

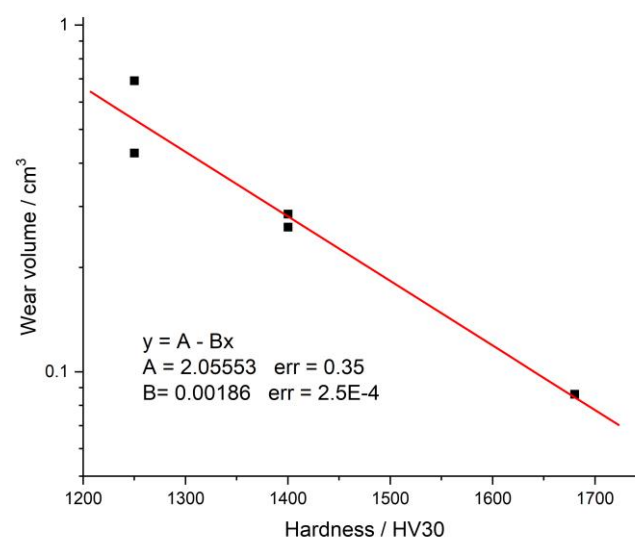


**Figure 3.** Wear volume vs. hardness characteristics for samples A–E of Table 1.

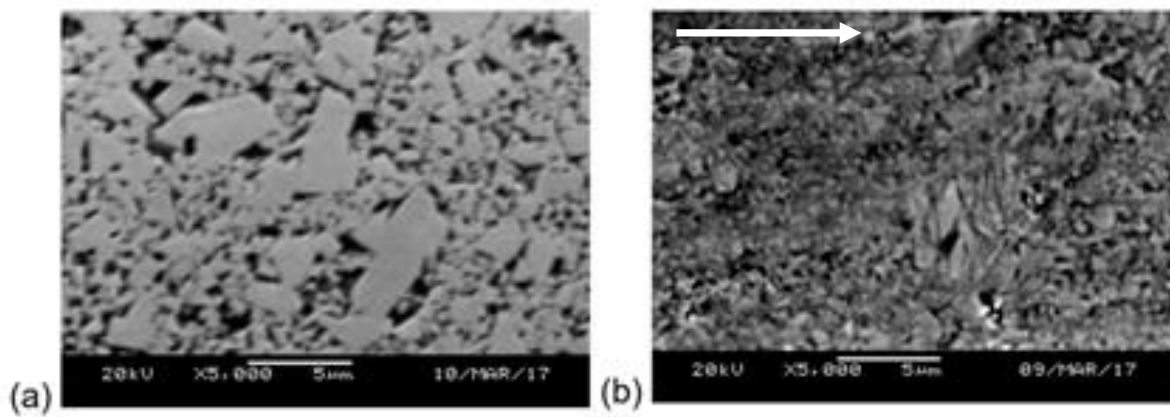


**Figure 4.** SEM micrographs of grade C of Table 1: (a) pristine surface, (b) after abrasion test (the arrow shows the friction direction).

### 3.1.2. Impact of Systematic Variations of Cr Content

Cr addition, keeping the content of the main component of the metallic binder constant, progressively increases the hardness (Figure 5a), always exhibiting a parabolic dependence [4,35]. The Ni-base grades obey a similar behaviour, highlighting a continuous increase in hardness with the increase of the Cr addition, even if the specific increment seems to be smaller. Furthermore, Ni-base grades show hardness values that are significantly lower than those of Co-base ones. The abrasion results of the investigated grades—compiled in Figure 5b—are coherent with the expected correlation with hardness values (Figure 5a): the amount of removed mass in each sample is inversely proportional to the hardness value. The same behaviour was also found for Ni-base grades, opening up the possibility of optimizing the choice of the most performing grade for applications where abrasion–corrosion conditions have to be faced. Figure 6 shows the results of the grain-size evaluation by the linear-intercept method. In spite of a quite large distribution, the mean values of grain size are consistent with a direct relationship with hardness and abrasion resistance. The hardening effect of the metallic binder alloy, resulting from Cr dissolution, cannot be definitively pinpointed on the basis of the available data alone and would require micro- or nano-indentation measurements on the phase. Nevertheless, one can notice that, as expected, in spite of the lower hardness, the mean WC grain size values of Ni-base grades are comparable to those of the Co-base ones with the same binder content. This result suggests that the Ni-base binder exhibits a lower hardness. As shown in Figure 7, in the 20 m% Co-base composition, Cr-additions to the binder which are larger than 5 m% cause the precipitation of free-C (Figure 7a, addition of 8 m% Cr). Moreover, for still higher Cr additions, both free-C and sub-micron Cr carbides (Figure 7b–d) are found, that, according to [25,36], should be  $M_7C_3$ . This result is also in agreement with calculations reported in [36]. The free-C precipitation could be caused by C availability from  $Cr_3C_2$ . The addition of 0.8 m% Cr as  $Cr_3C_2$  in a 20 m% Co grade, assuming that Cr is fully solubilized, means about 0.25 m% free-C availability over the whole composite. In Ni-base compositions, free-C precipitates appear with 8 and 10 m% Cr (Figure 8a), while Cr-carbides appear in the case of 12 and 15 m% Cr additions (Figure 8b), as shown by EDS (Figure 8c).

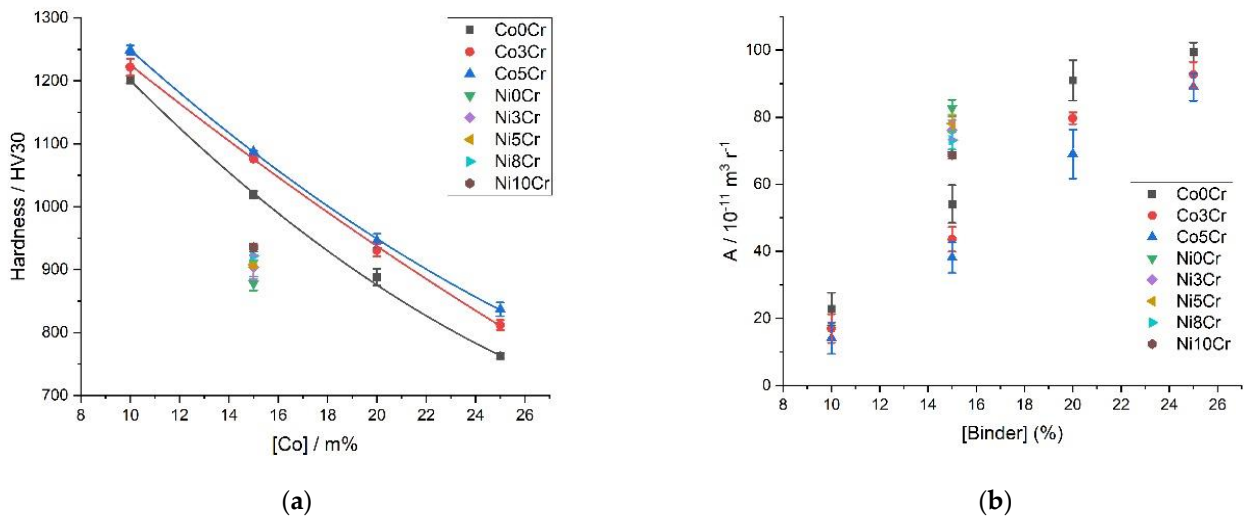


Figure 5. Dependence of hardness (a) and abrasion behaviour (ASTM B611) (b) on the amount of main component of the binder and of Cr (for details on samples, see Table 2).

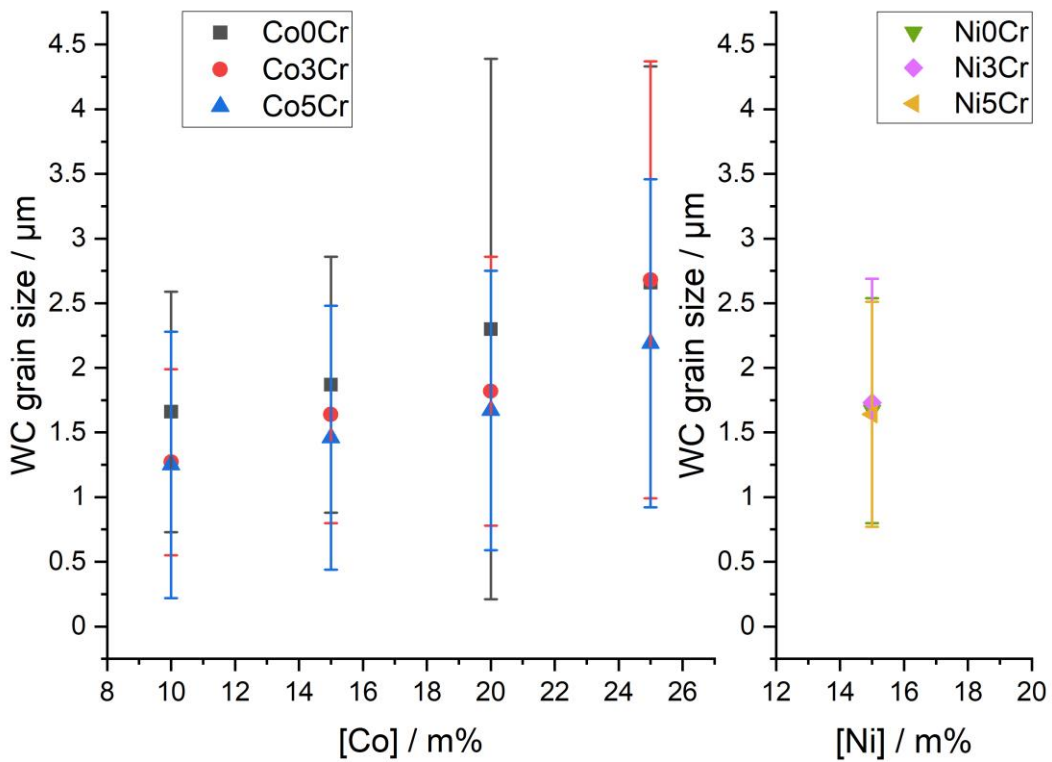
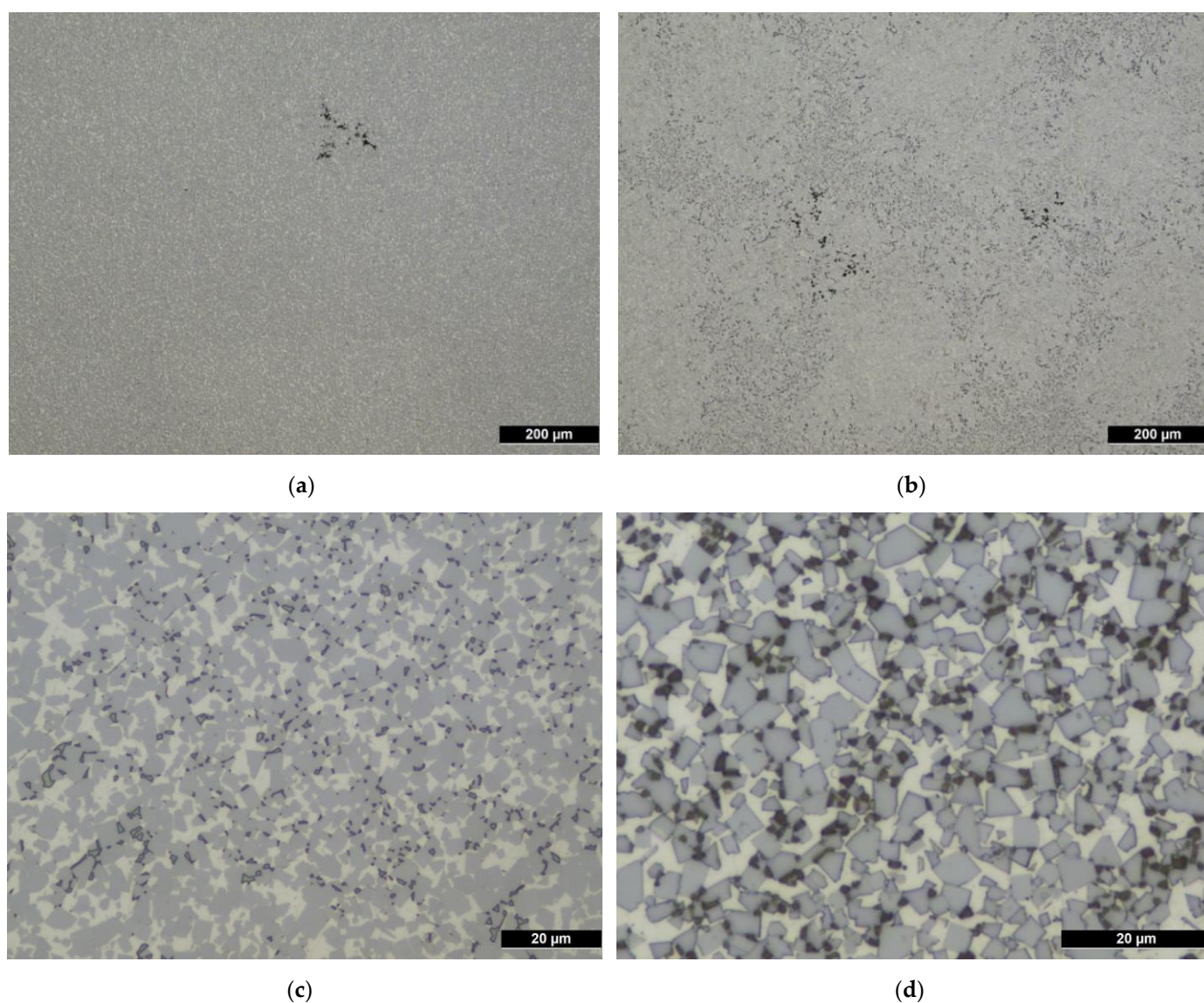


Figure 6. Mean WC grain size, evaluated by the linear intercept method [37]. For details of the samples, see Table 2.



**Figure 7.** Co-base grades: precipitation of free-C (a,b) and submicron sized Cr-carbides in grades with [Cr] > 8 m% (b–d). For details on the samples, see Table 2.

### 3.2. Corrosion Behaviour

#### 3.2.1. Co- and Ni-Based Grades with Cr, Hf and Ru Addition

As indicated in anticipation in Section 2.1, in view of Oil and Gas applications, it is important to rank CC grades with different Co- and Ni-based binder chemistries with specific additives. In particular, it is crucial to assess their relative responses under pure corrosion conditions in the absence of mechanical action. The key relevant corrosion conditions correspond to high oxidizing powers and the presence of high chloride concentrations. To this aim, we carried out systematic corrosion tests in  $\text{Na}_2\text{SO}_4$  solution, representative of non-marine industrial conditions, and in simulated seawater. The results of electrochemical measurements on samples A–E of Table 1 are shown in Figure 9. The anodic currents in neutral aqueous solution are notably higher in the absence of  $\text{Cl}^-$  for all the investigated grades, with the exception of sample C with a very high fraction of pure Co binder that exhibits the least noble Open Circuit Potential (OCP) value and corrosion current densities in excess of  $1 \text{ mA cm}^{-2}$  over the investigated potential range. In the NaCl solution, the pure-Co grades exhibit a PP feature, peaking at potentials that correlates clearly with the binder fraction. The Cr-doped CoNi grade with a high proportion of binder does not exhibit

propensity to PP (D), while the Cr-doped Ni-based binder is already pseudopassivated under OCP exposure conditions. All samples do not show transpassive behaviour in the absence of  $\text{Cl}^-$ , while in the presence of  $\text{Cl}^-$ , the transpassive potentials are similar and close to 0.75 V. Overall, from the LSV curves in the  $\text{Cl}^-$  solution, the following corrosion resistance ranking was found:  $E > A > B > C > D$ .

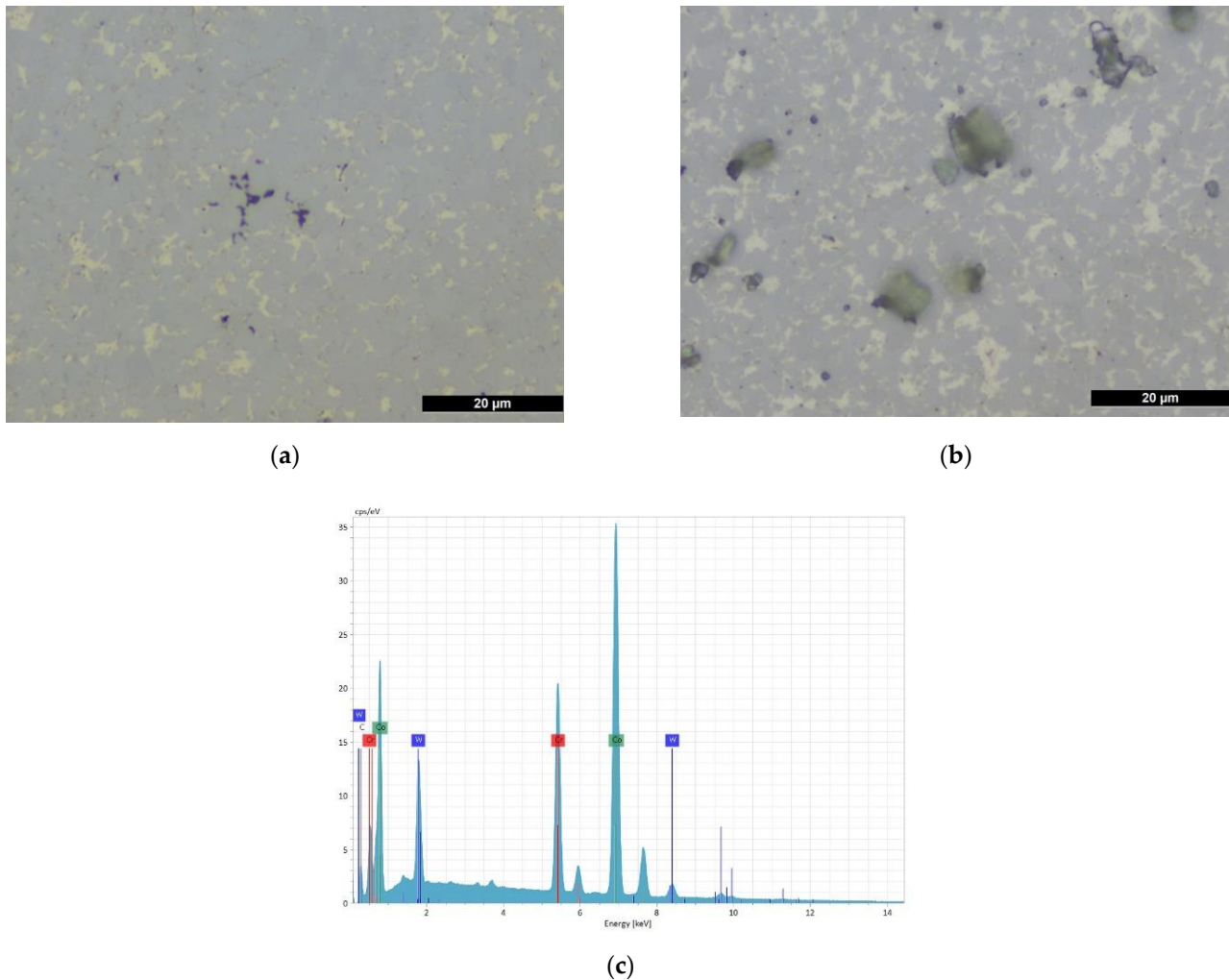


**Figure 8.** Ni-base grades: precipitation of free-C at  $[\text{Cr}] = 10 \text{ m}\%$  (a), Cr-carbides at  $[\text{Cr}] > 10 \text{ m}\%$  (b) and related EDS spectrum (c). For details on the samples, see Table 2.

On the basis of the ranking of anodic performance with respect to  $\text{Cl}^-$  content, we undertook a detailed study of the impact of binder compositional variations. Since the aggressiveness of  $\text{Cl}^-$  tends to smooth out subtle aspects of anodic response, we selected neutral 0.5 M  $\text{Na}_2\text{SO}_4$  as the test electrolyte for this purpose. The results of the OCP and LSV measurements for grades  $A_1$ – $E_1$  of Table 1 are given in Table 5 and Figure 10. Coherently with the relative nobility of Co and WC, it can be noticed that the amount of Co in the binder systematically anticorrelates with the electrochemical nobility of the grades. Noble Ru increases the nobility of the corresponding WC-Co grades by ca. 0.2 V, while baser Hf lowers the OCP value by ca. 0.1 V. The use of alloyed Ni (IN738LC superalloy) as the binder of WC results in the noblest grade of those investigated. The LSV curves show a critical impact of the binder chemistry on the PP behaviour. Figure 10 clearly shows the extension of the active range brought about by increasing the amount of Co. Panels (B) and (C) prove that alloying Co with either Hf or Ru leads to an improvement in corrosion performance: the latter, nobler alloying element affords a more effective protection. It is worth noting that the grade with the alloyed Ni binder exhibits a remarkable corrosion resistance. The

measured LSV were fitted with the models described in Section 2.5.2: the resistivity model (Section 2.5.2) was found to yield better matches with experimental data and was selected for systematic fitting work. As commented in Section 2.5.2, we were mainly interested in following the PP behaviour of CC grades and for this reason the transpassive region was not followed by the fit. In particular, the corrosion current of the bare material was able to be quantitatively extracted using this model and was used to define the effectively removed PPF fraction (see Sections 2.5.2 and 3.3.1 for details).

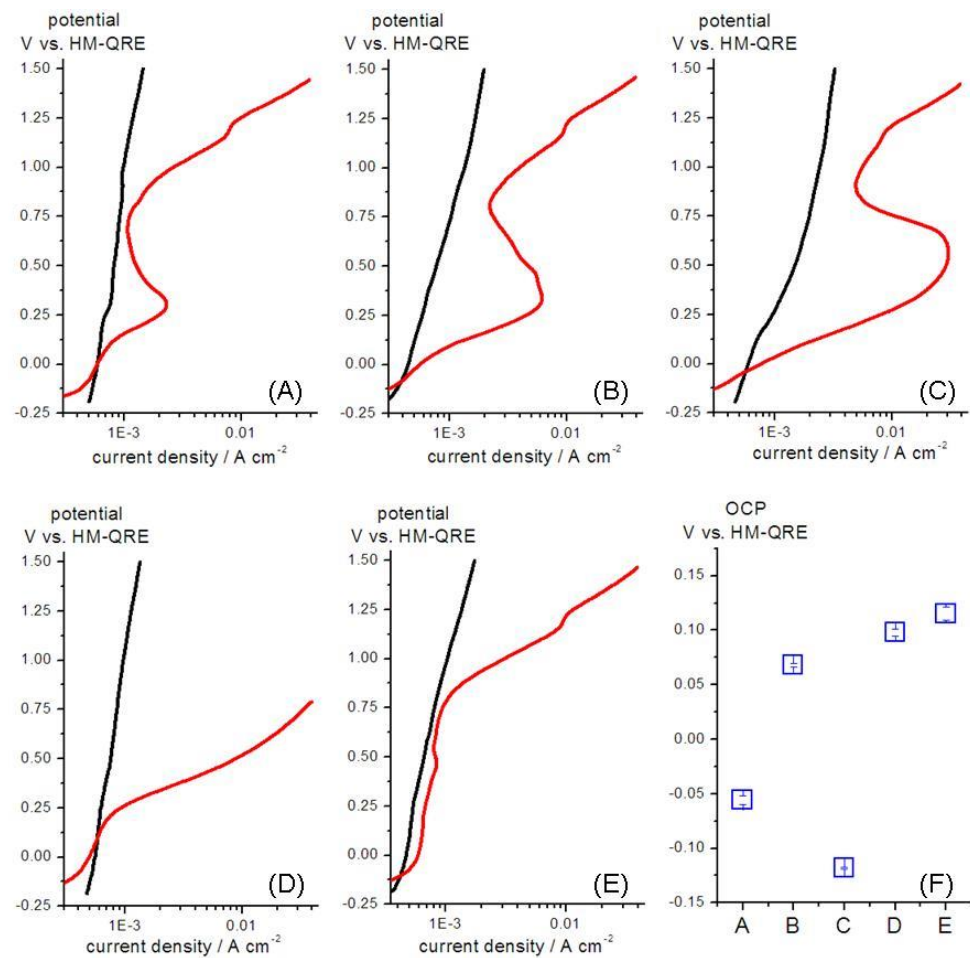


**Figure 9.** (A–E) LSV curves measured in tap water (black plots) and NaCl 0.6 M (red plots) of the grades listed in Table 1. Scan rate: 1 mV s<sup>-1</sup>. (F) Open circuit potential (OCP) values measured in tap water.

**Table 5.** Open circuit potential values of different CC grades in 0.5 M Na<sub>2</sub>SO<sub>4</sub>.

	WC-xCo	WC-xCo-1Ru	WC-xCo-0.5Hf	WC-9Ni <sub>alloyed</sub>
x = 6	-0.220 ± 0.006 V (samp. A <sub>1</sub> )	-0.100 ± 0.005 V (samp. C <sub>1</sub> )	-0.305 ± 0.001 V (samp. D <sub>1</sub> )	-
x = 9	-0.275 V (samp. B <sub>1</sub> )	-0.110 ± 0.006 V	-0.331 ± 0.014 V	-0.081 ± 0.002 V (samp. E <sub>1</sub> )
x = 12	-0.312 ± 0.007 V	-	-	-

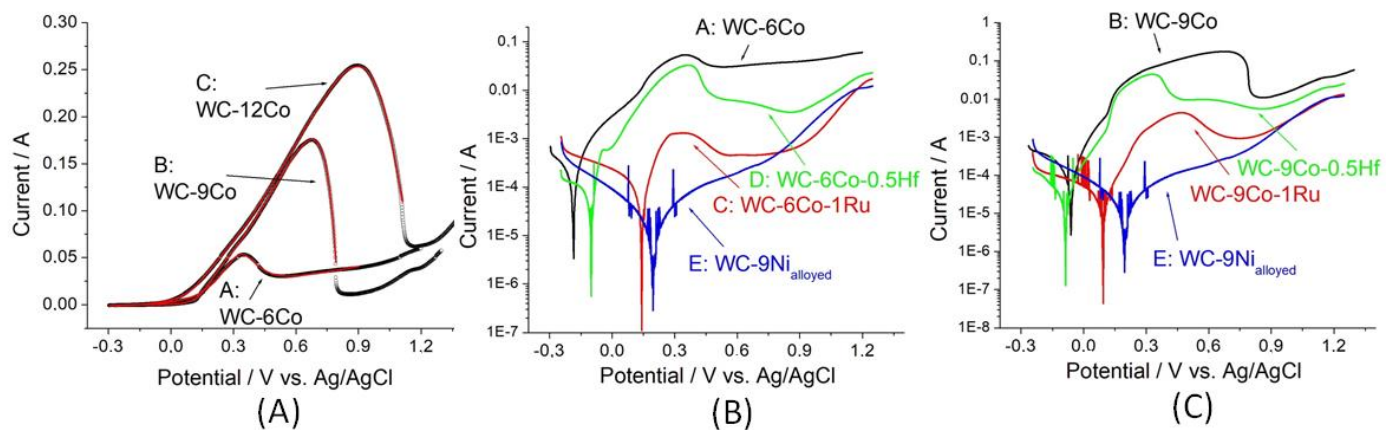


**Figure 10.** LSV curves of different CC grades in 0.5 M Na<sub>2</sub>SO<sub>4</sub>, scan rate: 1 mV s<sup>-1</sup>. (A) Effect of different Co binder fractions. The black plots are experimental curves, the red ones are fits (see text). (B,C) Impact of different binder compositions and fractions (indicated in the figure).

### 3.2.2. Impact of Systematic Variations of Cr Content

Corresponding to the literature ([38] and references therein) and on the basis of the greater insight acquired with the experiments described in Section 3.2.1, Cr was confirmed to exhibit a crucial role in the corrosion resistance of CC grades both in the absence and in the presence of Cl<sup>-</sup>. Notwithstanding the relatively clear understanding of the role of Cr, only scanty and scattered information is available on the synergy of Cr and other binder constituents. For this reason, we investigated the effect of systematic variations of Cr content on the corrosion performance of a representative range of binder compositions (see Table 2 for more details). For the reasons stated in the last paragraph of the previous section, we carried out electrochemical measurements in 0.5 mM Na<sub>2</sub>SO<sub>4</sub>, the results of which are reported in Figure 11. Cr additions evidently extend the PP range in all investigated cases. The apparent drop in the pseudopassive range extent upon increasing the Co content from 10% to 15% is due to the fact that, during the first LSV, the sample with a larger amount of Co still actively corrodes and a maximum, such as that measured with the sample with lower Co content, is therefore not expressed. Nevertheless, film-formation can still be assessed through the evident change in I-V slope. As far as the open-circuit potential (OCP) is concerned, the presence of Cr generally brings about alloy ennobling, with the exception of low-Co grades for which it exhibits a denobling effect, which might result from a subtle interaction of the W and Cr contents. Similarly, the Ni grade with a low amount of Cr (3%) is less noble than the corresponding Cr-free binder. Panel (F) of Figure 11 reports the current density measured for all grades at the potential at which the pseudopassivity of the Cr-free Co 10% grade breaks down (ca. 0.9 V<sub>Ag/AgCl</sub>). This electrochemical quantity can be considered as a parameter representative of corrosion resistance in oxidizing conditions, appropriate for hard metal ranking. From the dependence of this quantity on Cr content, it can be concluded that alloying with Cr appreciably lowers the corrosion current density in PP conditions. The only exception is the Ni grade with 3% Cr, in which a decrease in corrosion performance is found, coherently with the denobling of the OCP found for this alloy. In correspondence, a perturbation of the LSV curve is observed, while higher Cr contents bring about a qualitative change in the voltammetric behaviour. Thus, Cr seems to exhibit some type of threshold effect in both Co and Ni grades, possibly bearing an analogy with the behaviour of stainless steels, which would merit further investigation.

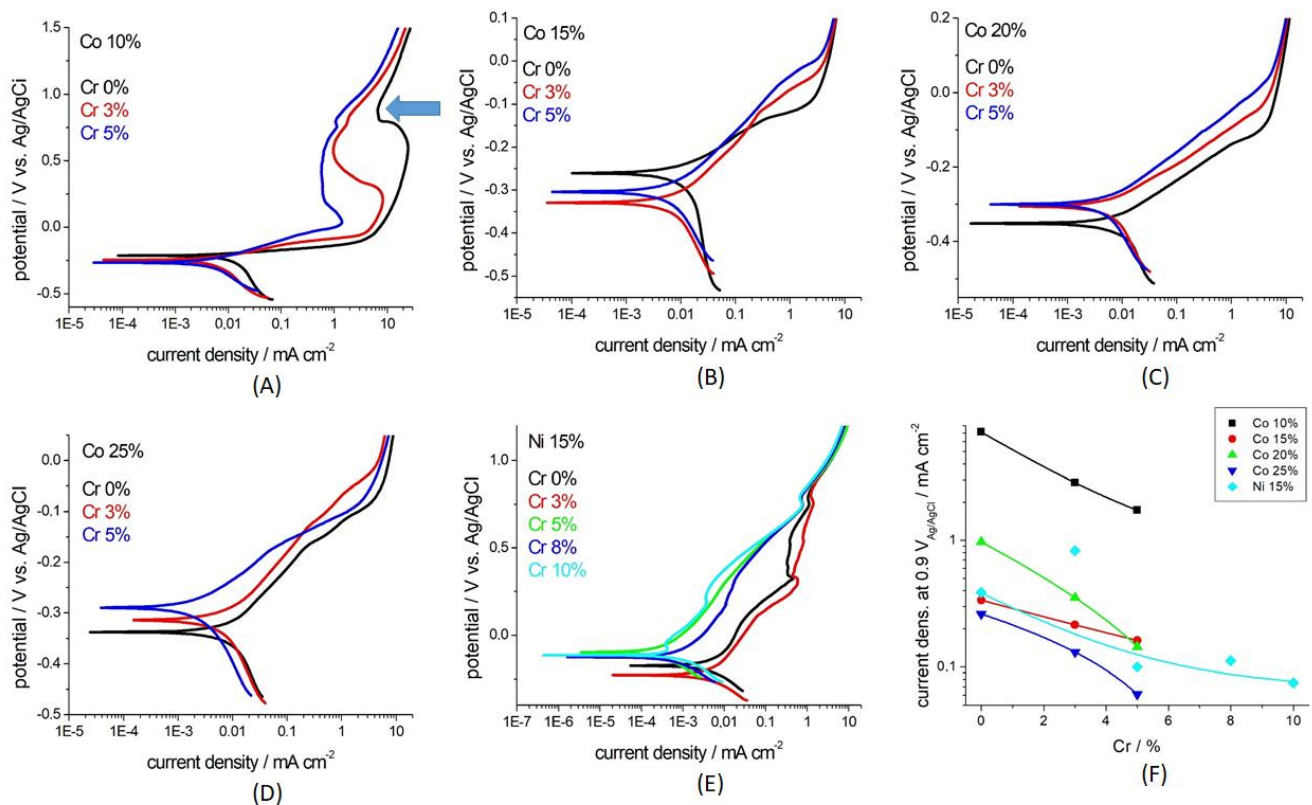


**Figure 11.** (A–E) LSV curves for the indicated Co- and Ni-base hard metal grades with Cr additions, in Na<sub>2</sub>SO<sub>4</sub> 0.5 M aerated aqueous solution (scan rate: 1 mV s<sup>-1</sup>). (F) The current density at 0.9 V<sub>Ag/AgCl</sub> for the investigated grade (i.e., the potential corresponding to the anodic end of the PP potential range of the Cr-free Co 10% grade, see grey arrow in Panel (A)).

### 3.3. Abrasion–Corrosion Behaviour

#### 3.3.1. Co- and Ni-Based Grades with Cr, Hf and Ru Addition

Potentials typical of fully developed PP conditions were selected for each material on the basis of the LSV results of Figure 9. A representative experimental result is shown in Figure 12. The current vs. time transients were elaborated with the approach described in Section 2.5.3. The abrasion–corrosion results are summarized in Figures 13 and 14, while the estimated time constants are listed in Table 6. Panels A and B of Figure 13 show that, upon starting the wheel rotation, a fast current transient occurs, corresponding to the removal of the PPF, followed by an approximately parabolic growth corresponding to the increase of sample area resulting from abrasion. The current increase from the plots of Panels (A) and (B) corresponds to the increase in surface area due to erosion. From the steady current increase time intervals, a ranking of the abrasion–corrosion resistance of the investigated grades can be straightforwardly established: D > A ≅ E > B ≅ C. The three better-performing grades not only exhibit lower currents but also a notably slower initial current increase, denoting the better resistance of the PPF towards mechanical removal by abrasion. The results highlight the role of the metallic binder content and composition, in particular the role of Ni and alloyed binders. The addition of NaCl during abrasion results in a dramatic current increase (see transition from the 3rd to the 4th interval in Figure 12, and Panel (C) of Figure 13) for all investigated grades. In correspondence, potential transients are observed exhibiting an initial drop, followed by a minimum. The initial fast drop corresponds to the enhancement of corrosion of the bare hard metal surface, triggered by the presence of Cl<sup>-</sup>: grades A, D and E exhibit a slower process, denoting lower propensity to active dissolution. Again, the role of the metallic binder is highlighted. The subsequent maximum is due to the formation of a dynamic interface resulting in a limited degree of protection: grade A is the most effective for developing this

kind of behaviour, while grade E supports a high corrosion rate with a very low applied potential. Thus, abrasion in the presence of NaCl results in a change of the ranking of the abrasion–corrosion resistance of the investigated grades:  $B \gg A \cong E \cong D \gg C$ . Resuming abrasion in the presence of  $\text{Cl}^-$  after an interval in which the rotation of the wheel is stopped does not change the grade ranking (Figure 13d). It is worth observing that a maximum can be observed only upon injecting  $\text{Cl}^-$ : this suggests that a stable chloride-modified corrosion product layer forms. Moreover, the slower-reacting grades (A, D and E) still shows longer time constants for the initial potential drop. In response to the hexane addition during abrasion in the  $\text{Cl}^-$ -containing solution (Figure 13e), the potential is slightly increased for all grades, indicating a decrease of corrosion rate, probably related to the fact that the volume fraction of water-insoluble hydrocarbon translates into a corresponding fraction of poorly conducting electrolyte. The addition of hexane during abrasion does not affect the hierarchy of potential levels and transition rates among grades determined by  $\text{Cl}^-$ . Figure 14A shows the electrochemical relaxation taking place after stopping the wheel rotation in tap water, corresponding to a drop current due to the reformation of the PPF. The hierarchy of corrosion currents after stopping abrasion is similar to that found during abrasion, with a slight improvement of the behaviour of grade E, which seems to show better PP behaviour, irrespective of the aggression conditions and probably as a consequence of the higher electrochemical potential of the metallic binder. As one can appreciate from Table 6, the time constants are grouped into three levels: faster for B (ca. 4 s); intermediate for A, C and E (ca. 15 s); and slower for D (ca. 20 s). Interestingly, relaxation after abrasion in the presence of  $\text{Cl}^-$  (Panel (B)) exhibits the notably varied behaviour of the investigated materials: grades A, B, D and E show a current drop, while hard metal C shows a slow increase to a current level over one order of magnitude higher than the initial one. The ranking of electrochemical corrosion performance in the presence of  $\text{Cl}^-$  changes profoundly between abrading and non-abrading conditions: in the former case—as discussed above—we find  $B \gg A \cong E \cong D \gg C$ , but after stopping the wheel we obtain  $A \cong E > B \gg D \gg C$ , with a dramatic decrease of the corrosion resistance of grade C. A similarly complex scenario is found after ceasing abrasion in the presence of both NaCl and hexane: in this case, all grades exhibit a current density decrease and the hierarchy of corrosion resistance is different under abrasion or after stopping it, where the following relative values are found:  $A \cong E > B \gg C > D$ .

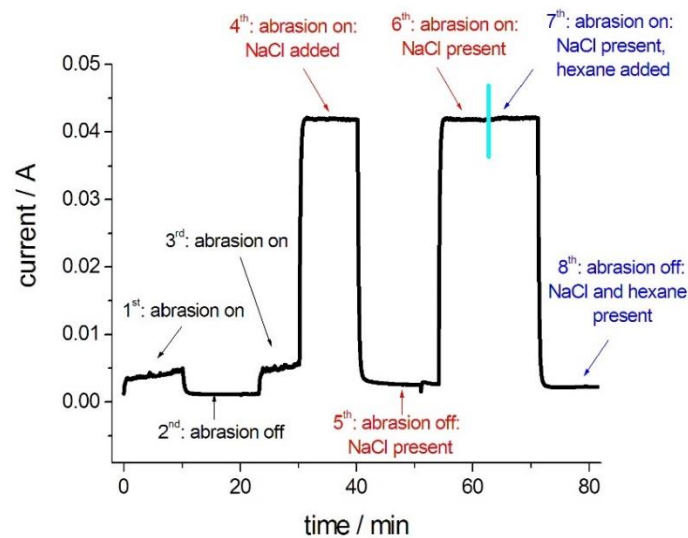


**Figure 12.** A typical abrasion–corrosion testing sequence under electrochemical control, see Section 3.3 for details.

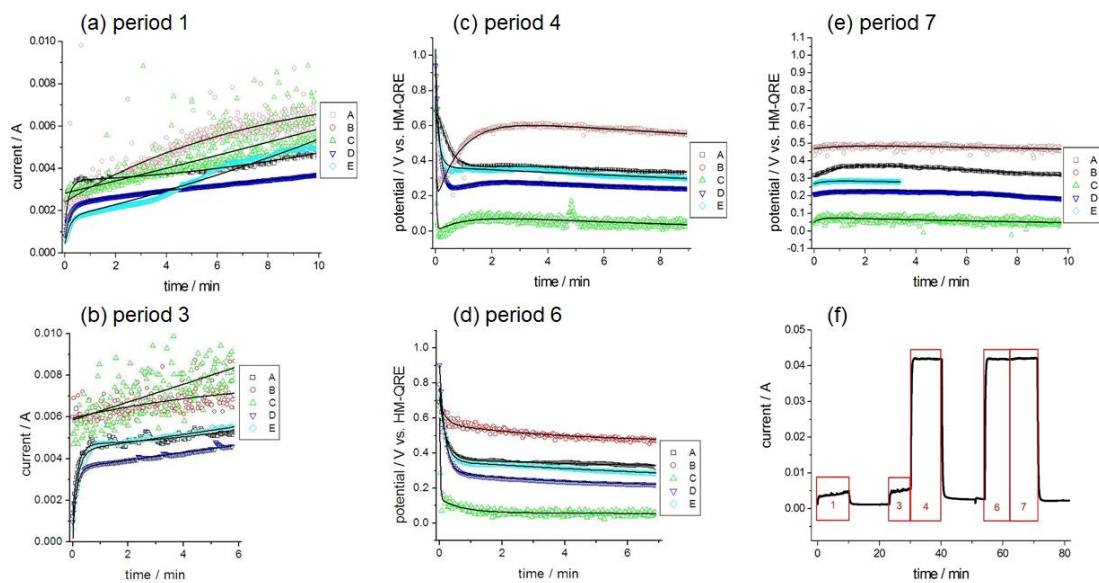


**Figure 13.** Electrochemical transients corresponding to the onset of abrasion or to the injection of chemicals for the grades A–E, as detailed in Table 1. The electrochemical testing of the different grades was carried out using the following potentials: A, 0.70  $V_{\text{HM-QRE}}$ ; B, 0.80  $V_{\text{HM-QRE}}$ ; C, 1.0  $V_{\text{HM-QRE}}$ ; D, 0.90  $V_{\text{HM-QRE}}$ ; and E, 0.75  $V_{\text{HM-QRE}}$ . (a,b) Onset of abrasion in tap water; (c) NaCl injection during abrasion; (d) onset of abrasion in the presence on NaCl; (e) hexane injection. Scatter plots correspond to experimental data, continuous lines are best fits. Panel (f) shows the collocation of the transients displayed in Panels (a–e).

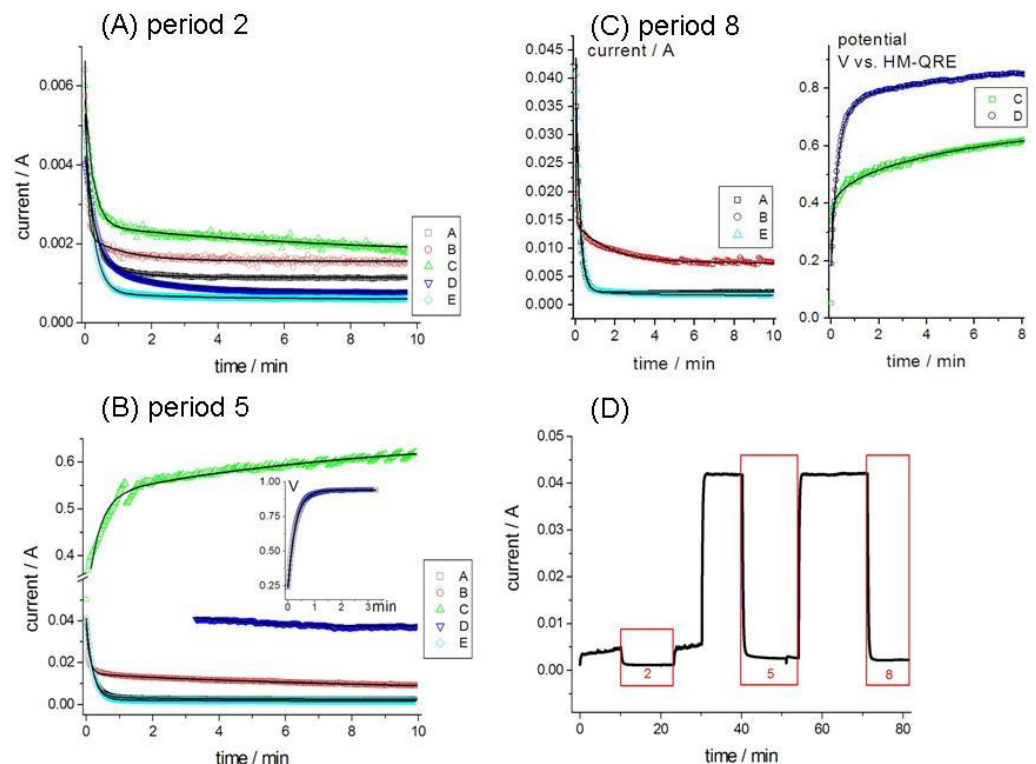


**Figure 14.** Electrochemical transients corresponding to the interruption of abrasion. (A) Tap water; (B) in presence of NaCl, since grade D undergoes a shift from galvanostatic to potentiostatic control during relaxation (see text for details), the potential transient is shown in the inset; (C) in presence of NaCl and hexane. Scatter plots correspond to experimental data, continuous lines are best fits. Panel (D) shows the exact collocation in the time of the transients.

**Table 6.** Time constants estimated from the transients depicted in Figures 13 and 14  $\pm$  95% confidence intervals. In the few cases in which the objective function is shallow in the neighbourhood of the minimum and the confidence interval estimates are thus very large, these have been simply omitted.

	A	B	C	D	E
1st	0.170 $\pm$ 0.010 + parabola	7.603 $\pm$ 1.024 + line	fast rise + line	0.203 $\pm$ 0.001 + line	0.2 + parabola
2nd	0.222 $\pm$ 0.003 0.934 $\pm$ 0.044	0.065 $\pm$ 0.002 1.139 $\pm$ 0.052	0.246 $\pm$ 0.007 8.165 $\pm$ 1.101	0.326 $\pm$ 0.003 1.922 $\pm$ 0.034	0.245 $\pm$ 0.001 2.574 $\pm$ 0.147
3rd	0.183 $\pm$ 0.008 + parabola	6.314 $\pm$ 3.173	fast rise + line	0.154 $\pm$ 0.002	0.173 $\pm$ 0.002 + line
4th	0.255 $\pm$ 0.083 + parabola	0.028 $\pm$ 0.002 0.886 $\pm$ 0.027 56.77 $\pm$ 3.07	0.023 $\pm$ 0.001 1.198 $\pm$ 0.288 8.401 $\pm$ 1.103	0.164 $\pm$ 0.002 0.988 $\pm$ 0.667 50.58 $\pm$ 9.49	0.134 $\pm$ 0.003 43.52 $\pm$ 27.76
5th	0.188 $\pm$ 0.001 2.628 $\pm$ 0.057	0.093 $\pm$ 0.002 6,448 $\pm$ 0.251	0.023 $\pm$ 0.008 0.356 $\pm$ 0.020 8.230 $\pm$ 1.558	0.282 $\pm$ 0.001 4.809 38.55	0.198 $\pm$ 0.001 3.115 $\pm$ 0.174
6th	0.221 $\pm$ 0.002 8.756 $\pm$ 0.220	0.199 $\pm$ 0.029 4.014 $\pm$ 0.177	0.023 $\pm$ 0.002 0.734 $\pm$ 0.163 14.33	0.177 $\pm$ 0.000 4.726 $\pm$ 0.046	0.187 $\pm$ 0.001 17.17 $\pm$ 0.10
7th	0.982 $\pm$ 0.020 40.25 $\pm$ 0.380	1.093 $\pm$ 0.250 173.9 $\pm$ 19.40	0.224 $\pm$ 0.094 20.54 $\pm$ 1.64	3.287 $\pm$ 0.272 22.81 $\pm$ 0.960	0.374 $\pm$ 0.023 128.7 $\pm$ 10.10
8th	0.197 $\pm$ 0.001	0.034 $\pm$ 0.001 1.696 $\pm$ 0.027	0.031 $\pm$ 0.003 0.509 $\pm$ 0.112 5.425 $\pm$ 0.402	0.218 $\pm$ 0.008 0.515 $\pm$ 0.043 6.112 $\pm$ 0.406	0.209 $\pm$ 0.001 3.152 $\pm$ 0.416

To deepen the understanding of the impact of binder composition on abrasion–corrosion, beyond the ranking proposed above in this section, we carried out a detailed study of the effect of Ru and Hf as well as of Co-binder content (specimens A<sub>1</sub>–D<sub>1</sub> of Table 1). As already discussed in the case of pure corrosion, the impact of Cl<sup>−</sup> is so strong that subtle material effects can be better appreciated with a Cl<sup>−</sup>-free electrolyte: again, we selected 0.5 M Na<sub>2</sub>SO<sub>4</sub>. In this case, in which sensitivity to mechanical action is more important than to electrochemical attack, the abrasion–corrosion tests were performed with the following sequence: the total duration of the abrasion–corrosion test (10 min) was divided into three intervals, two of 3 min and one of 4 min. At the beginning and at the end of each test and between successive rotation periods, 10 min relaxation periods were allowed in order to follow the restoration of PPF. During the test, a potentiostatic (+0.5 V) current was recorded. This potential was chosen as representative of PP conditions for all the investigated grades immersed in 0.5 M Na<sub>2</sub>SO<sub>4</sub>. The results of the potentiostatic measurements are shown in Figure 15. The impact of the presence or absence of the abrading action on the corrosion current is pretty obvious, as well as the fact that the individual grades exhibit notably different dynamic responses. The common qualitative aspects of the abrasion transient are of course dictated by the removal of the PPF upon inception of the wheel rotation—yielding a current increase—and by its reformation upon cessation of abrasion, resulting in a current relaxation to values that are typical of the PP voltammetric range. In order to obtain quantitative information, the current transients were again elaborated according to the method expounded in Section 2.5.3: the extracted time constants are listed in Table 7, together with the computed removed effective PPF fraction  $R_{PP}$ . From the comparison of data in Tables 6 and 7, a clear correlation emerges between Vickers hardness and the  $R_{PP}$ ,  $\tau_{\uparrow 1}$  and  $\tau_{\uparrow 2}$  parameters extracted from the abrasion–corrosion measurements, while  $\tau_{\downarrow 1}$  and  $\tau_{\downarrow 2}$  seem to depend exclusively on the nature of the material. In particular,  $R_{PP}$  and  $\tau_{\uparrow 1}$  are anticorrelated with HV, while  $\tau_{\uparrow 2}$  is positively correlated. The negative correlation between HV and  $\tau_{\uparrow 1}$  can be explained by considering that, in the materials considered in this study, the harder materials are also the more corrosion-resistant, as a result

of the chemical action of the additive. In fact, the PP currents of Figure 10 and the current values before abrasion inception in Figure 15 perfectly correlate with hardness. Since better PPFs are also thinner, they are more quickly removed by the abrading action. The positive correlation of HV and  $\tau_{\uparrow 2}$  simply depends on the fact that the resistance of the grade to mechanical damaging is better for the harder materials. The positive correlation of HV and  $R_{PP}$ , results from the synergy of high corrosion resistance and lower wear rate of the harder grades. As far as the bi-exponential current decay is concerned, it can instead be observed that  $\tau_{\downarrow 1}$  and  $\tau_{\downarrow 2}$  are notably faster for the Ru-containing grades, with decay rates correlating positively with the fraction of Ru in Co, suggesting that the noble element improved the repassivation ability. Concerning Hf, it exhibits the longest  $\tau_{\downarrow 1}$  value and an intermediate  $\tau_{\downarrow 2}$  one, while among the WC-Co grades, faster repassivation is found for the higher-Co grade, possibly owing to a faster corrosion product release. It is worth noting that, upon varying the nature of the binder, apart from the case of the Hf-containing grade—which contains a secondary phase— $\tau_{\downarrow 1}$  and  $\tau_{\downarrow 2}$  vary in the same direction, suggesting that in binders containing the alloying element in solid solution, the PPF formation and growth rates are controlled by the same process.

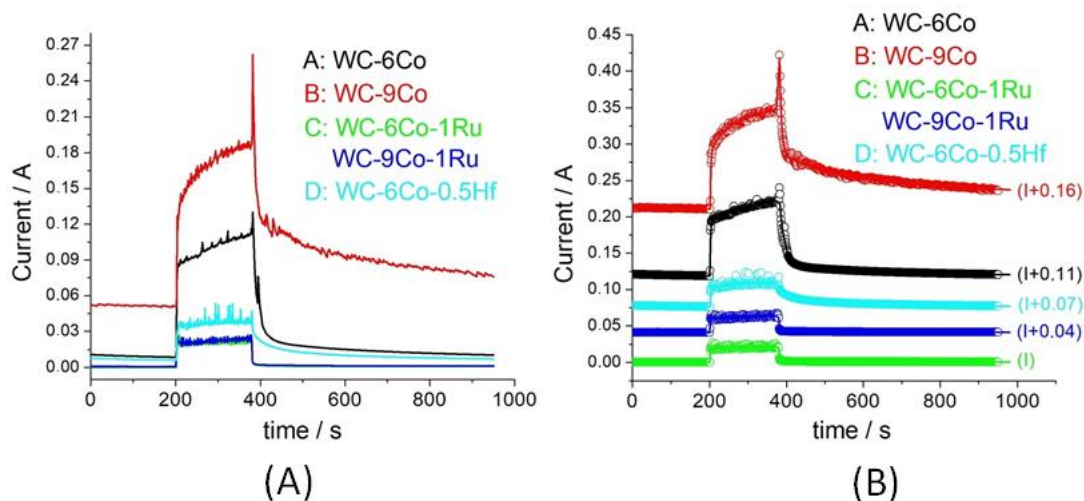


**Figure 15.** A selection of abrasion–repassivation transients measured in 0.5 M Na<sub>2</sub>SO<sub>4</sub> at 0.5 V vs. HM-QRE (A) and their fits (B), for the indicated set of samples listed in Table 1. For more details, refer to text.

**Table 7.** Parameters extracted from quantitative analyses of the abrasion–repassivation transients of Figure 15.

Grade	$R_{PP}$ (%)	$\tau_{\uparrow 1}$ (s)	$\tau_{\uparrow 2}$ (s)	$\tau_{\downarrow 1}$ (s)	$\tau_{\downarrow 2}$ (s)
A: WC-6Co	$3.75 \pm 0.34$	$1.70 \pm 0.21$	$238.0 \pm 11.0$	$13.13 \pm 0.93$	$278.0 \pm 12.0$
B: WC-9Co	$5.41 \pm 0.67$	$2.03 \pm 0.13$	$69.0 \pm 7.6$	$5.096 \pm 0.771$	$227.0 \pm 8.0$
C: WC-6CoRu	$0.365 \pm 0.023$	$0.97 \pm 0.10$	$257.0 \pm 14.0$	$0.690 \pm 0.103$	$28.8 \pm 1.7$
WC-9CoRu	$0.453 \pm 0.065$	$1.12 \pm 0.25$	$262.0 \pm 21$	$0.739 \pm 0.094$	$109 \pm 8.0$
D: WC-6CoHf	$0.946 \pm 0.134$	$0.97 \pm 0.07$	$257.0 \pm 12$	$24.44 \pm 1.55$	$200.0 \pm 7$

### 3.3.2. Impact of Systematic Variations of Cr Content

Since repassivation under free-corrosion conditions is the single most informative parameter for Cr-containing grades, the resistance of which depends on surface enrichment with Cr [38], we chose to carry out abrasion–corrosion tests by recording OCP transients in the 0.5 M Na<sub>2</sub>SO<sub>4</sub> electrolyte (Figure 16). A systematic denobling of the mixed potential is evident, which can be straightforwardly explained by the removal of the oxidized surface layer. The sequence of OCP results is preserved in both static and abrading conditions. In

addition, it can be noticed that Ni-base grades exhibit lower denobling degrees than the corresponding Co-base ones. These results confirm the outstanding effect of Cr additions and the role of Ni as a metallic binder in aggressive environments, counteracting the relatively poor abrasion resistance of the Ni-base grades.

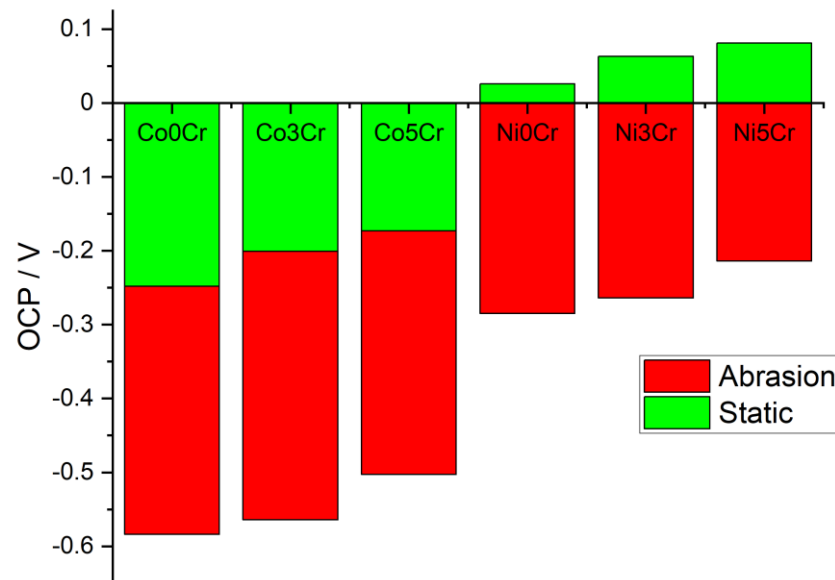


**Figure 16.** OCP values under static and abrasion conditions (mean values are reported on the plot, the standard deviation is always lower than 10 mV).

#### 4. Conclusions

In this study we have analysed the electrochemical corrosion response to the application of abrasion conditions of a range of wear-resistant WC-Co type hard metals with different amounts of Co, Ni and Cr and the addition of Ru and Hf as solid-solution and secondary-phase hardeners. Moreover, the effect of metallic binder content and tungsten carbide grain size distribution were considered. In addition, the contribution of the environment chemistry was assessed: a three-phase fluid (seawater, liquid hydrocarbon and sand) was simulated, and the effects of the constituents was studied by subsequent additions.

A device for abrasion–corrosion tests was developed, based on the ASTM B611 steel wheel rig, incorporating three-electrode electrochemical control of the specimens subjected to abrasion. This rig enables the investigation of the synergistic action of abrasion and corrosion, focussing both on stationary and transient regimes. Abrasion–corrosion electrochemical transients were modelled with an electrokinetic model that allows, on the one hand, to separately quantify the pure PP behaviour and the abrasion contributions to the corrosion current and, on the other hand, to model and predict their synergy.

The results of this study highlight the role of the metallic binder content and composition, showing the relevance of binder alloying with Ni and Cr. In particular, results on alloyed-Ni (IN738LC) binders bear the promise of outstanding abrasion–corrosion performance. We also pinpointed that Ru additions allow an exceptional improvement of the corrosion and abrasion–corrosion resistance of Co-based grades. HfC additions also afford an improvement of both corrosion and abrasion–corrosion, though not as remarkable as with Ru.

In general, we can thus draw the following conclusions. (i) An appropriate choice of additives can lead to the improvement of both corrosion resistance and mechanical properties, specifically hardness and toughness. (ii) The increase of abrasion–corrosion performance is chiefly determined by hardness. (iii) Repassivation kinetics are the key aspect controlling the corrosion contribution to abrasion–corrosion through self-healing capabilities: this was found to be an intrinsic material property that can be tuned by additives.

**Author Contributions:** Conceptualization, B.B. and G.P.D.G.; methodology, B.B.; software, F.T.; validation, B.B. and G.P.D.G.; formal analysis, B.B.; investigation, F.T. and S.T.; resources, S.T.; data curation, F.T.; writing—original draft preparation, B.B. and G.P.D.G.; writing—review and editing, B.B. and G.P.D.G.; visualization, F.T.; supervision, B.B.; project administration, S.T.; funding acquisition, G.P.D.G. All authors have read and agreed to the published version of the manuscript.

**Funding:** This research received no external funding.

**Data Availability Statement:** No data are reported.

**Conflicts of Interest:** The authors declare no conflict of interest.

## References

1. Ettmayer, P.; Kolaska, H.; Ortner, H.M. History of Hardmetals. In *Comprehensive Hard Materials—Hardmetals, Ceramics, Super Hard Materials*; Mari, D., Llanes, L., Nebel, C.E., Eds.; Elsevier: Amsterdam, The Netherlands, 2014.
2. Wright, I.G.; Shetty, D.K.; Clauer, A.H. A comparison of the slurry erosion behaviour of WC-Co cermets and ceramics. In Proceedings of the Conference 11th International Plansee Seminar, Reutte, Austria, 20–24 May 1985; Bildstein, H., Ortner, H., Eds.; Plansee Metalwerke: Reutte, Austria, 1985; Volume 2, p. 643.
3. Gee, M.G.; Gant, A.J.; Roebuck, B.; Mingard, K.P. Wear of Hardmetals. In *Comprehensive Hard Materials—Hardmetals, Ceramics, Super Hard Materials*; Mari, D., Llanes, L., Nebel, C.E., Eds.; Elsevier: Amsterdam, The Netherlands, 2014.
4. De Gaudenzi, G.P.; Bozzini, B. Meccanismi di corrosione del metallo duro. *Metall. Ital.* **2017**, *11*, 39.
5. De Gaudenzi, G.P.; Amati, M.; Gianoncelli, A.; Gregoratti, L.; Kiskinova, M.; Kourousias, G.; Tedeschi, S.; Bozzini, B. The spatial organization of corrosion products at the hardmetal/environment interface. In Proceedings of the 20th International Plansee Seminar, Reutte, Austria, 30 May–3 June 2022; Wex, K., Kestler, H., Pilz, A., Eds.; Plansee Group Functions Austria GmbH: Reutte/Tyrol, Austria, 2022.
6. Mischler, S.; Debaud, S.; Landolt, D. Wear-Accelerated Corrosion of Passive Metals in Tribocorrosion Systems. *J. Electrochem. Soc.* **1998**, *145*, 750. [[CrossRef](#)]
7. Mischler, S.; Spiegel, A.; Landolt, D. The role of passive oxide films on the degradation of steel in tribocorrosion systems. *Wear* **1999**, *225*, 1078–1087. [[CrossRef](#)]
8. Mischler, S.; Spiegel, A.; Stemp, M.; Landolt, D. Influence of passivity on the tribocorrosion of carbon steel in aqueous solutions. *Wear* **2001**, *251*, 1295. [[CrossRef](#)]
9. Landolt, D.; Mischler, S.; Stemp, M. Electrochemical methods in tribocorrosion: A critical appraisal. *Electrochim. Acta* **2001**, *46*, 3913. [[CrossRef](#)]
10. Wood, R.J.K.; Sun, D.; Thakare, M.R.; de Frutos Rozas, A.; Wharton, J.A. Interpretation of electrochemical measurements made during micro-scale abrasion-corrosion. *Tribol. Int.* **2010**, *43*, 1218. [[CrossRef](#)]
11. Thakare, M.R.; Wharton, J.A.; Wood, R.J.K.; Menger, C. Exposure effects of alkaline drilling fluid on the microscale abrasion-corrosion of WC-based hardmetals. *Wear* **2007**, *263*, 125. [[CrossRef](#)]
12. Spriggs, G.E. A history of fine grained hardmetal. *Int. J. Refract. Met. Hard Mater.* **1995**, *13*, 241. [[CrossRef](#)]
13. Exner, H.E.; Gurland, J. A review of parameters influencing some mechanical properties of tungsten carbide-cobalt alloys. *Powder Metall.* **1970**, *13*, 13–31. [[CrossRef](#)]
14. Tracey, V.A.; Hall, N.R.V. Nickel matrices in cemented carbides. *Powder Metall. Int.* **1980**, *12*, 132.
15. Ekemar, S.; Lindholm, L.; Hartzell, T. Nickel as a binder in WC-based cemented carbides. *Int. J. Refract. Met. Hard Mater.* **1982**, *3*, 37.
16. Adorjan, A.; Schubert, W.; Schön, A.; Bock, A.; Zeiler, B. WC grain growth during the early stages of sintering. *Int. J. Refract. Met. Hard Mater.* **2006**, *24*, 365. [[CrossRef](#)]
17. Garcia, J.; Ciprés, V.C.; Blomqvist, A.; Kaplan, B. Cemented carbide microstructures: A review. *Int. J. Refract. Met. Hard Mater.* **2019**, *80*, 40. [[CrossRef](#)]
18. Warbichler, P.; Hofer, F.; Grogger, W.; Lackner, A. EFTEM-EELS characterization of VC and Cr<sub>3</sub>C<sub>2</sub> doped cemented carbides. In Proceedings of the 15th International Plansee Seminar, Reutte, Austria, May 2001; Kneringer, G., Rodhammer, P., Wildner, H., Eds.; Plansee AG: Reutte, Austria, 2001; Volume 2, p. 65.
19. Delanoe, A.; Lay, S. Evolution of the WC grain shape in WC-Co alloys during sintering: Cumulated effect of the Cr addition and of the C content. *Int. J. Refract. Met. Hard Mater.* **2009**, *27*, 189. [[CrossRef](#)]
20. Llanes, L.; Casas, B.; Idáñez, E.; Marsal, M.; Anglada, M. Surface Integrity Effects on the Fracture Resistance of Electrical-Discharge-Machined WC-Co Cemented Carbides. *J. Am. Ceram. Soc.* **2004**, *87*, 1687–1693. [[CrossRef](#)]
21. Human, A.M.; Roebuck, B.; Exner, H.E. Electrochemical polarisation and corrosion behaviour of cobalt and Co(W,C) alloys in 1 N sulphuric acid. *Mater. Sci. Eng. A* **1998**, *241*, 202. [[CrossRef](#)]
22. Bozzini, B.; Busson, B.; de Gaudenzi, G.P.; Humbert, C.; Mele, C.; Tedeschi, S.; Tadjeddine, A. Corrosion of cemented carbide grades in petrochemical slurries. Part I—Electrochemical adsorption of CN<sup>−</sup>, SCN<sup>−</sup> and MBT: A study based on in situ SFG. *Int. J. Refract. Met. Hard Mater.* **2016**, *60*, 37. [[CrossRef](#)]

23. Santos, R.F.; Rocha, A.M.F.; Bastos, A.C.; Cardoso, J.P.; Rodrigues, F.; Fernandes, C.M.; Sacramento, J.; Ferreira, M.G.S.; Senos, A.M.R.; Fonseca, C.; et al. The effect of Cr content on the corrosion resistance of WC-Ni-Cr-Mo composites. *Int. J. Refract. Met. Hard Mater.* **2021**, *95*, 105434. [[CrossRef](#)]
24. Motitschka, R.; Ettmayer, P.; Kny, E. Constitution of the Systems Co-Cr-W-C and Ni-Cr-W-C in the Cobalt and Nickel Corner. In Proceedings of the 12th International Plansee Seminar, Reutte, Tirol, Austria, 8–12 May 1989; Bildstein, H., Ortner, H.M., Eds.; Metallwerk Plansee GmbH: Reutte, Austria, 1989; Volume 2, p. 863.
25. Zackrisson, J.; Jansson, B.; Uphadyaya, G.S.; Andrén, H.-O. WC-Co based cemented carbides with large Cr<sub>3</sub>C<sub>2</sub> additions. *Int. J. Refract. Met. Hard Mater.* **1998**, *16*, 417. [[CrossRef](#)]
26. Markström, A.; Norgren, S.; Frisk, K.; Jansson, B.; Sterneland, T. Experimental and thermodynamic evaluation of the Co-Cr-C system. *Int. J. Mater. Res.* **2006**, *97*, 1243. [[CrossRef](#)]
27. Kaplan, B.; Norgren, S.; Schwind, M.; Selleby, M. Thermodynamic calculations and experimental verification in the WC-Co-Cr cemented carbide system. *Int. J. Refract. Met. Hard Mater.* **2015**, *48*, 257. [[CrossRef](#)]
28. De Calderon, R.; Edtmaier, C.; Schubert, W.-D. Novel binders for WC-based cemented carbides with high Cr contents. *Int. J. Refract. Met. Hard Mater.* **2019**, *85*, 105063. [[CrossRef](#)]
29. Steinlechner, R.; de Oro Calderon, R.; Koch, T.; Linhardt, P.; Schubert, W.D. A study on WC-Ni cemented carbides: Constitution, alloy compositions and properties, including corrosion behaviour. *Int. J. Refract. Met. Hard Mater.* **2022**, *103*, 105750. [[CrossRef](#)]
30. Lisovskii, A.F. Cemented carbides alloyed with ruthenium, osmium and rhenium. *Powder Metall. Met. Ceram.* **2000**, *39*, 428. [[CrossRef](#)]
31. Shing, T.L.; Luyckx, S.; Northrop, I.T.; Wolff, I. The effect of ruthenium additions on the hardness, toughness and grain size of WC-Co. *Int. J. Refract. Met. Hard Mater.* **2001**, *19*, 41. [[CrossRef](#)]
32. Bonjour, C.; Actis-Data, A. Effects of ruthenium additions on the properties of WC-Co ultra micrograins. In Proceedings of the Conference Euro PM2004, Vienna, Austria, 17–21 October 2004; EPMA: Shewsbury, UK, 2004; Volume 3.
33. Ettmayer, P. Hardmetals and cermets. *Annu. Rev. Mater. Sci.* **1989**, *19*, 145. [[CrossRef](#)]
34. Gant, A.J.; Gee, M.G.; Roebuck, B. Rotating wheel abrasion of WC/Co hardmetals. *Wear* **2005**, *258*, 178. [[CrossRef](#)]
35. Kim, C.-S. Microstructural-Mechanical Properties Relationship in WC-Co Composites. Ph.D. Thesis, Carnegie Mellon University, Pittsburgh, PA, USA, 2004.
36. Frisk, K.; Markström, A. Effect of Cr and V on phase equilibria in Co-WC based hardmetals. *Int. J. Mater. Res.* **2008**, *99*, 287. [[CrossRef](#)]
37. *ISO 4499-2:2008; Hardmetals—Metallographic Determination of Microstructure—Part 2: Measurement of WC Grain Size.* ISO: Geneva, Switzerland, 2008.
38. Bozzini, B.; Gianoncelli, A.; Kourousias, G.; Boniardi, M.; Casaroli, A.; Zilio, S.D.; Hussain, R.; Abyaneh, M.K.; Kiskinova, M.; Mele, C.; et al. The role of chromium in the corrosion performance of cobalt- and cobalt-nickel based hardmetal binders: A study centred on X-ray absorption microspectroscopy. *Int. J. Refract. Met. Hard Mater.* **2020**, *92*, 105320. [[CrossRef](#)]